Electronic Supplementary Information

High-efficiency organic solar cells from low-cost pentacyclic fused-ring electron acceptors via crystal engineering

Wenkui Wei, Xiyue Yuan, Jianbin Zhong, Zhiqiang Wang, Xia Zhou, Feixiang Zhao, Dinglong Feng, Yue Zhang, Weidi Chen, Mingqun Yang, Wei Zhang,* Zaifei Ma, Zheng Tang, Xinhui Lu, Fei Huang, Yong Cao, and Chunhui Duan**

1. Experimental Procedures

1.1 Synthesis and characterization

General information: 4,7-Dibromo-2-butyl-5,6-dinitro-2H-benzo[d][1,2,3]triazole (1) and tributyl(4-octylthiophen-2-yl)stannane (2) were synthesized according to the reported literatures.[1, 2] Polymer donor PBDCT was synthesized by modifying the reported polymer donor PBCT-2F to adjust the solubility and energy level for organic solar cell applications.[3, 4] The synthetic details of the polymer donor PBDCT will be reported elsewhere. The other chemicals and solvents were purchased from commercial companies and used as received unless otherwise indicated.

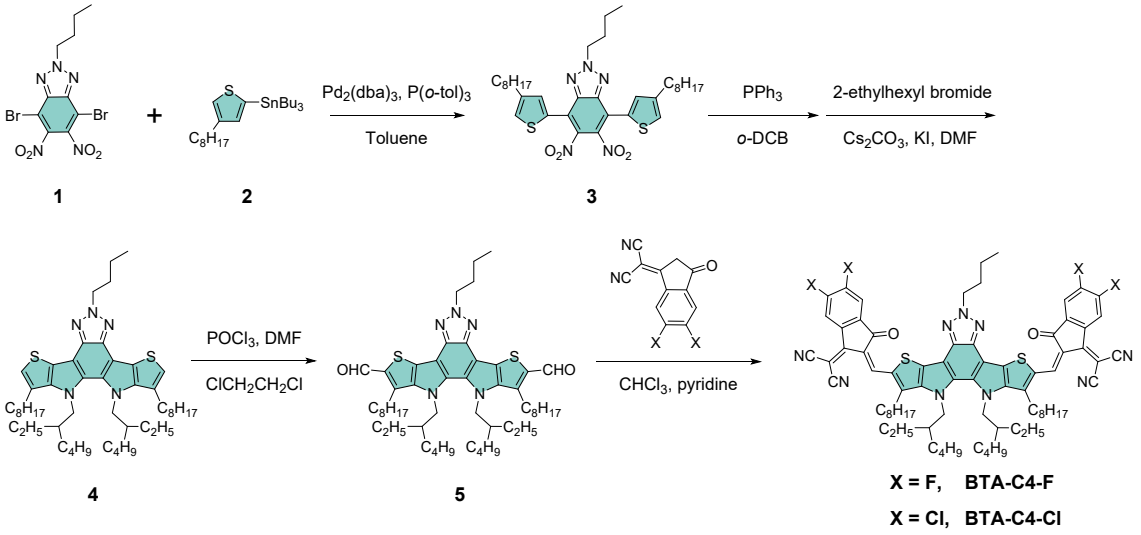

Scheme S1. Synthetic routes of BTA-C4-F and BTA-C4-Cl.

Synthesis of compound 3: Compound 1 (900 mg, 2.13 mmol), compound 2 (2.27 g, 4.68 mmol), $Pd_2(dba)_3$ (97.41 mg, 0.11 mmol), and P(*o*-tol)$_3$ (130 mg, 0.43 mmol) were dissolved in

dry toluene (80 mL) and stirred at 110 °C overnight. The mixture was cooled to room temperature and then concentrated under reduced pressure. The crude product was purified by silica gel column with the solvent mixture of dichloromethane/petroleum ether (1/10, *v*/*v*) as eluent to afford compound 3 as an orange oil (1.14 g, 82% yield). ^{1}H NMR (500 MHz, $CDCl_3$, δ, ppm): 7.33 (s, 2H), 7.24 (s, 2H), 4.81 (t, J = 9.05 Hz, 2H), 2.65 (t, J = 9.35 Hz, 4H), 2.13 (m, 2H), 1.65 (m, 5H), 1.40–1.28 (m, 21H), 0.99 (m, 3H), 0.88 (m, 6H). ^{13}C NMR (125 MHz, $CDCl_3$, δ, ppm): 144.32, 141.67, 139.67, 131.54, 129.34, 125.42, 119.54, 57.75, 31.89, 31.87, 30.36, 30.32, 29.43, 29.28, 26.94, 22.69, 19.74, 14.13, 13.43.

Synthesis of compound 4: Compound 3 (1.10 g, 1.68 mmol) and PPh_3 (4.41 g, 16.8 mmol) were dissolved in 1,2-dichlorobenzene (*o*-DCB, 13 mL) and refluxed for 16 hours at 180 °C under nitrogen atmosphere. The mixture was cooled to room temperature and then concentrated under reduced pressure. After removing the solvent, the dark green residue was added into a three-necked round bottom flask without further purification. Then, KI (279 mg, 1.68 mmol), Cs_2CO_3 (2.19 g, 6.73 mmol) and 2-ethylhexyl bromide (1.30 g, 6.73 mmol) were dissolved in *N*,*N*-dimethylformamide (DMF, 40 mL). The reaction was stirred under nitrogen at 80 °C for 12 hours, and then cooled to room temperature. The organic layer was extracted by dichloromethane and dried over anhydrous $MgSO_4$. The crude product was purified by silica gel column with the solvent mixture of dichloromethane/petroleum ether (1/8, *v*/*v*) as eluent to afford compound 4 as a greenish yellow oil (851 mg, 62% yield). ^{1}H NMR (500 MHz, $CDCl_3$, δ, ppm): 6.98 (s, 2H), 4.80 (t, J = 9.30 Hz, 2H), 4.46 (d, 4H), 2.90 (t, J = 9.25 Hz, 4H), 2.19 (m, 2H), 1.86 (m, 4H), 1.59 (m, 6H), 1.43–1.30 (m, 19H), 1.01–0.53 (m, 38H).

Synthesis of compound 5: To a mixture of dry 1,2-dichloroethane (20 mL) and anhydrous DMF (5 mL), $POCl_3$ (1 mL) was added under nitrogen atmosphere and then stirred at −10 °C for 2 hours. The solution of compound 4 (850 mg, 1.04 mmol) in dry 1,2-dichloroethane (20 mL) was added slowly under nitrogen protection. The reaction was stirred at 80 °C for 4 hours. Then, 20 mL water was added, and the reaction was stirred overnight. The organic layer was extracted by dichloromethane and dried over $MgSO_4$. The crude product was purified by silica gel column with the solvent mixture of ethyl acetate/petroleum ether (1/30, *v*/*v*) as eluent to afford compound 5 (763 mg, 84% yield). ^{1}H NMR (500 MHz, $CDCl_3$, δ, ppm): 10.14 (s, 2H), 4.81 (t, J = 9.15 Hz, 2H), 4.47 (s, 4H), 3.52–3.07 (d, 2H), 2.19 (m, 2H), 1.88 (m, 4H), 1.63 (mi,

2H), 1.47–0.88 (m, 48H), 0.45–0.19 (m, 11H). ^{13}C NMR (125 MHz, $CDCl_3$) δ: 182.33, 144.66, 143.17, 138.93, 137.60, 136.16, 136.01, 110.19, 56.07, 52.94, 47.97, 40.45, 32.23, 31.88, 31.47, 29.57, 29.49, 29.22, 27.07, 22.64, 19.98, 14.08, 13.63.

Synthesis of BTA-C4-F: To a 100 mL two-necked flask, compound 6 (220 mg, 0.25 mmol), 2-(5,6-difluoro-3-oxo-2,3-dihydro-1*H*-inden-1-ylidene)malononitrile (232 mg, 1.00 mmol), and dried chloroform (40 mL) were added. The mixture was degassed by nitrogen for 15 minutes. Then 1 mL of pyridine was added. The mixture was stirred at 65 °C for 9 hours. After cooling to room temperature, the mixture was poured into 100 mL methanol and the precipitate was collected by filtration. The crude product was purified with column chromatography on silica gel using the solvent mixture of dichloromethane/petroleum ether (1/1, *v*/*v*) as the eluent. Then the final product was obtained by recrystallization from chloroform/methanol solvent mixture, yielding a dark blue solid (269 mg, 82%). ^{1}H NMR (500 MHz, $CDCl_3$, *δ*, ppm): 9.21 (s, 2H), 8.58 (s, 2H), 7.73 (s, 2H), 4.84 (t, *J* = 7.30 Hz, 2H), 4.51 (s, 4H), 3.52–3.16 (d, 4H), 2.24 (m, 2H), 1.85 (m, 4H), 1.66 (m, 2H), 1.50 (m, 6H) 1.35–1.27 (m, 25H), 1.06–0.87 (m, 16H), 0.47–0.16 (m, 12H). ^{13}C-NMR (125 MHz, $CDCl_3$, *δ*, ppm): 185.83, 159.47, 155.50, 153.40, 146.31, 143.76, 138.20, 137.68, 136.59, 136.16, 136.06, 135.74, 134.65, 120.44, 115.28, 115.01, 112.63, 112.21, 68.17, 56.35, 52.95, 40.42, 32.27, 32.09, 31.90, 31.60, 29.68, 29.56, 29.23, 28.01, 25.37, 23.73, 22.64, 20.01, 14.13, 14.08, 13.66, 11.02, 7.94. MALDI-TOF: calcd. for $C_{76}H_{83}F_4N_9O_2S_2$ (M^+): 1294.67; found: 1294.27.

Synthesis of BTA-C4-Cl: BTA-C4-Cl was obtained by following the similar procedure for the synthesis of BTA-C4-F with 2-(5,6-dichloro-3-oxo-2,3-dihydro-1*H*-inden-1-ylidene)malononitrile as end-capping reagent. The crude product was purified with column chromatography on silica gel using the solvent mixture of dichloromethane/petroleum ether (1/1, *v*/*v*) as the eluent. Then the final product was obtained by recrystallization from chloroform/methanol solvent mixture, yielding a dark blue solid (288 mg, 85%). ^{1}H NMR (500 MHz, $CDCl_3$, *δ*, ppm): 9.24 (s, 2H), 8.81 (s, 2H), 7.99 (s, 2H), 4.84 (t, *J* = 7.35 Hz, 2H), 4.51 (s, 4H), 3.52–3.15 (d, 4H), 2.25 (m, 2H), 1.85 (m, 4H), 1.66 (m, 2H), 1.50 (m, 6H), 1.35–1.27 (m, 25H), 1.06–0.87 (m, 16H), 0.63–0.16 (m, 12H). ^{13}C-NMR (125 MHz, $CDCl_3$, *δ*, ppm): 185.89, 159.34, 146.43, 143.91, 139.42, 139.22, 138.70, 138.32, 138.03, 136.44, 136.25, 136.18, 126.87, 125.10, 120.46, 115.36, 114.73, 112.34, 68.22, 56.37, 53.07, 40.43, 32.25,

32.11, 31.89, 31.60, 29.68, 29.57, 29.23, 28.04, 25.40, 23.68, 22.63, 20.01, 14.13, 14.08, 13.66, 11.04, 7.97. MALDI-TOF: calcd. for $C_{76}H_{83}Cl_4N_9O_2S_2$ (M^+): 1360.48; found: 1360.27.

1.2 Measurements and characterization

Nuclear magnetic resonance (NMR): ^1H and ^{13}C NMR were measured on a Bruker AV-500 MHz spectrometer in deuterated chloroform solution at room temperature. Chemical shifts (δ) were recorded with tetramethylsilane (TMS) as the internal standard.

MALDI-TOF-MS: MALDI-TOF-MS measurements were performed on Bruker Daltronik GmbH (autoflex II) under positive ion mode with dithranol as matrix.

Thermogravimetric analyses (TGA): TGA was measured on NETZSCH (TG 209 F3) at a heating rate of 10 °C min^{-1} with a nitrogen gas flow.

UV-*vis*-NIR absorption spectra: UV-*vis*-NIR spectra were recorded on a Shimadzu UV-3600 spectrophotometer at room temperature. All UV-*vis*-NIR experiments for solutions were performed in chloroform with the sample concentration of 0.02 mg mL^{-1}. Films were prepared by spin coating the chloroform solutions onto glass substrates.

Electrochemical cyclic voltammetry (CV): CV measurements were performed on a CHI660A electrochemical workstation in a solution of tetrabutylammonium hexafluorophosphate (Bu_4NPF_6, 0.1 M) in acetonitrile at a scan rate of 50 mV s^{-1}. Glassy carbon electrode, platinum wire and an Ag/AgCl electrode were used as working electrode, counter electrode, and reference electrode, respectively.

DFT calculation: The geometry was fully optimized at the B3LYP/6-311G+(d, p) level of theory by the absence of imaginary frequencies. The long alkyl side-chains were simplified by methyl groups for saving the computation time. All calculations were carried out with the Gaussian 16 software.[5] The ESP and excited state analysis were carried out by a wavefunction analysis tool Multiwfn.[6]

Grazing incidence wide angle X-ray scattering (GIWAXS): GIWAXS measurements were carried out with a Xeuss 2.0 SAXS/WAXS laboratory beamline using a Cu X-ray source (8.05 keV,1.54 Å) and a Pilatus3R 300 K detector. The incidence angle is 0.2°. The thin film samples (including neat and blend films) were prepared on Si wafer substrates by spin coating.

Single crystal X-ray diffraction: Single crystal of BT-F was obtained from the literature[2a] and those of BTA-C4-F and BTA-C4-Cl were obtained by slow diffusion of methanol or ethanol into its saturated chloroform solution. After the slow solvent evaporation in two weeks at room temperature, crystals were precipitated. A suitable crystal was selected and measured on Rigaku XtaLAB P2000 diffractometer. The crystal was kept at 150 K during data collection. After data reduction, the structure was solved with the ShelXT structure solution program using Intrinsic Phasing and refined with the ShelXL refinement package using Least Squares minimization. Hydrogen atoms are frequently placed on geometrically calculated positions and then refined using a "riding model" by "HFIX" command in ShelXL program, where the X−H bond lengths and H−X−H angles are usually given as constraints.

Synthetic complexity (SC) analysis: The synthetic complexity (SC) of acceptor materials was assessed by following the protocol reported by Po et al.[7] There are five parameters: (1) the number of synthetic steps (NSS), (2) the reciprocal yields of the monomers (RY), (3) the number of unit operations required for the isolation/purification of the monomers (NUO), (4) the number of column chromatographic purifications required by the monomers (NCC), (5) the number of hazardous chemicals used for their preparation (NHC). The SC can be calculated according to the following equation: $SC = 35\frac{NSS}{NSS_{max}} + 25\frac{RY}{RY_{max}} + 15\frac{NUO}{NUO_{max}} + 15\frac{NCC}{NCC_{max}} + 10\frac{NHC}{NHC_{max}}$, and an empirical coefficient was assigned to each parameter, which accounts for the relative importance. The weight of NSS, RY, NUO, NCC, and NHC is 35, 25, 15, 15, and 10, respectively.

Femtosecond transient absorption characterization: TA measurements were conducted by a home-built measurement system. This system is driven by a commercial femtosecond (fs) laser with a repetition rate of 1 kHz, pulse duration of ~170 fs and a wavelength of 800 nm. The amplifier (Legend Elite F 1K HE+II, Coherent, California, USA) is seeded by an oscillator (Mira-HP, Coherent, California, USA) running at 80 MHz. The fundamental laser was split into two beams. One is used to pump a home-built non-collinearly optical parametric amplifier, output of which is used to pump the samples of interest. The pump beam was modulated by a mechanic chopper (MC2000B-EC, Thorlabs, Newton, New Jersey) with a frequency of 500 Hz. The other beam is employed to generate the super-continuum white light, which is used as the

probe beam for differential absorption measurements, by focusing onto a sapphire plate. The probing light was guided into a monochromator (Omni-λ200i, Zolix, Beijing, China) and detected by a CCD detector (Pascher Instruments, Lund, Sweden). The time delay between the pump and probe beams is controlled by a mechanical delay line. For TA measurements, all samples were mounted into an optical chamber filled with nitrogen.

Exciton diffusion length measurement: The exciton diffusion length (L_d) was calculated by the equation, $L_d = (3D\tau)^{1/2}$, where τ is the exciton lifetime and D is the diffusion coefficient. According to the three-dimensional exciton diffusion model, D can be given by $D = \gamma/8\pi R$, where γ is the bimolecular exciton annihilation rate constant, R is the singlet-exciton annihilation radius that is generally assumed to be 1 nm. Assuming that annihilation destroys both excitons, the exciton decay dynamics characterized by TA spectroscopy can be globally fitted to a rate equation: $n(t) = \frac{n(0)exp(-kt)}{1+\frac{\gamma}{2k}n(0)[1-exp(-kt)]}$, where $n(t)$ is the singlet exciton density as a function of time after excitation, and k is the monocular fluorescence decay rate constant that can be obtained by the equation of $k = 1/\tau$.

PL experiments: Emission spectra were recorded on an Edinburgh Instruments FLSP920 double-monochromator spectrophotometer.

Atomic force microscopy (AFM): AFM images were acquired by using a Bruker Multimode 8 Microscope AFM in tapping-mode.

Transmission electron microscope (TEM): TEM images were obtained from a JEM-2100F transmission electron microscope operated at 200 kV.

1.3 Device fabrication and characterization

Fabrication of organic solar cells: Indium tin oxide-coated (ITO-coated) glass substrates were successively precleaned with isopropanol, detergent, de-ionized water, and isopropanol. After that, the clean substrates were dried in blast oven at 70 °C. Then, the substrates were subjected to oxygen plasma treatment for 3 minutes. Then poly(3,4-ethylenedioxythiophene):poly(styrenesulfonate) (PEDOT:PSS) (CLEVIOS™ PVP AI 4083 from Heraeus) was spin-coated on the ITO glass substrates at 3000 rpm for 40 seconds to give a thickness of 40 nm, followed by baking at 140 °C for 15 minutes. The substrates were

transferred to a nitrogen-filled glove box. For the optimal binary OSCs, the treatments of corresponding active layer were listed in Table S7−S9. Afterwards, a layer of PDINN (aliphatic amine-functionalized perylene-diimide)[8] was spin-coated from a methanol solution (1.0 mg mL^{-1}) at a spin speed of 3000 rpm for 30 seconds. Finally, a layer of Ag (100 nm) was thermally evaporated at a pressure of 4×10^{-7} Torr with a shadow mask.

Current density–voltage (*J*−*V*) characteristics: *J*–*V* curves were measured on a computer-controlled Keithley 2400 source meter under 1 sun, AM1.5 G spectrum from solar simulator (Enlitech, Taiwan), the light intensity was 100 mW cm^{-2} as calibrated by using a China General Certification Centre (CGC) certified reference monocrystal silicon cell (Enlitech), and the irradiation area of solar simulator was 12 × 12 cm^2. Before the *J*–*V* test of small area devices, a physical mask containing an aperture with a precise area of 4 mm^2 was used to define the device area.

External quantum efficiency (EQE): EQE spectra were recorded on a commercial EQE measurement system (Enlitech, QE-R3011, Taiwan). The light intensity at each wavelength was calibrated by a standard single-crystal Si photovoltaic cell.

Fabrication and characterization of single-carrier devices: Space-charge-limited-current (SCLC) hole and electron mobilities were acquired through the hole-only devices with a configuration of ITO/PEDOT:PSS/active layer/MoO_3/Ag and electron-only devices with a configuration of ITO/ZnO/active layer/PDINN/Ag, respectively. The dark current densities of the single-carrier devices were measured by using a computer-controlled Keithley 2400 source meter under nitrogen atmosphere.

Charge carrier mobility estimation: The charge carrier mobility was estimated by fitting the data acquired from single carrier devices to a SCLC model. The data was analyzed according to the Mott–Gurney law that considers a Poole–Frenkel-type dependence of mobility on the electric field, $J = \frac{9}{8}\varepsilon_r\varepsilon_0\mu_0\frac{V^2}{d^3}exp(0.891\gamma\sqrt{\frac{V}{d}})$, where ε_0 is permittivity of free space, ε_r is the dielectric constant of the polymer which is assumed to be 3 for organic semiconductors, μ_0 is the zero-field mobility, V is the voltage drop across the device, d is the film thickness of the active layer, and γ is a parameter that describes the strength of the field-dependence effect. The

hole and electron mobilities are extracted with the fit parameters at an electric field (E) of 2 × 10^5 V cm^{-1} by the Murgatroyd equation $\mu(E) = \mu_0 \exp(\gamma\sqrt{E})$.

Light-intensity dependence measurements: The light-intensity dependence measurements were carried out with illumination between 10–100 mW cm^{-2}, which was calibrated by a standard single crystal silicon solar cell (Enlitech). The current density and voltage were recorded with a Keithley 2400 source meter.

Impedance spectroscopy: The impedance spectroscopy was conducted on an impedance analyzer (KEYSIGHT E4990A). The ε_r of acceptor material was measured using impedance spectroscopy with the parallel-plate capacitance devices (ITO/PEDOT:PSS/test film/PDINN/Ag). The ε_r value can be obtained from the equation: $\varepsilon_r = \frac{Cd}{\varepsilon_r A}$, where C is the measured capacitance, ε_0 is the permittivity of free space (8.854 × 10^{-12} F m^{-1}), A is the device area, and d is the thickness of the test film.

Highly sensitive EQE_{PV} measurements: The EQE_{PV} spectra were measured by a highly sensitive home-build setup, which consisted of a halogen lamp (LSH-75, 250 W, Newport), an optical chopper and a monochromator (CS260-RG-3-MC-A, Newport), a phase-locked amplifier (SR830, Stanford Instrument) and a current amplifier (SR570, Stanford Instrument). A series of long-pass filters (600 nm, 900 nm, 1000 nm) were used to block the overtone signals from the monochromator. Calibration of the light intensity was performed using a standard Si detector (Hamamatsu s1337-1010BR). A background illumination of 100mWcm^{-2} was applied during the measurements. The illuminated area was approximately 0.5 mm^2, achieved through the use of a focus lens and an optical aperture.

EL measurements: EL spectra were recorded using a source meter (Keithley 2400) to inject electric current into the solar cell. A fluorescence spectrometer (KYMERA-3281-B2, Andor) with two sets of diffraction gratings, coupled to a Si EMCCD camera (DU970P-BVF, Andor) for the wavelength range of 400–1000nm, and an InGaAs camera (DU491A-1.7, Andor) for the wavelength range of 900–1700nm was used to collect the photons emitted from the solar cell.

EQE_{EL} measurements: EQE_{EL} measurements were perform educing a home-built setup. A digital source meter (Keithley2400) was used to inject electric current into the devices, and the

emitted photons are collected by a Si diode. The current generated by the Si diode was measured by a picoammeters (Keithley 6482).

2. Additional figures and tables

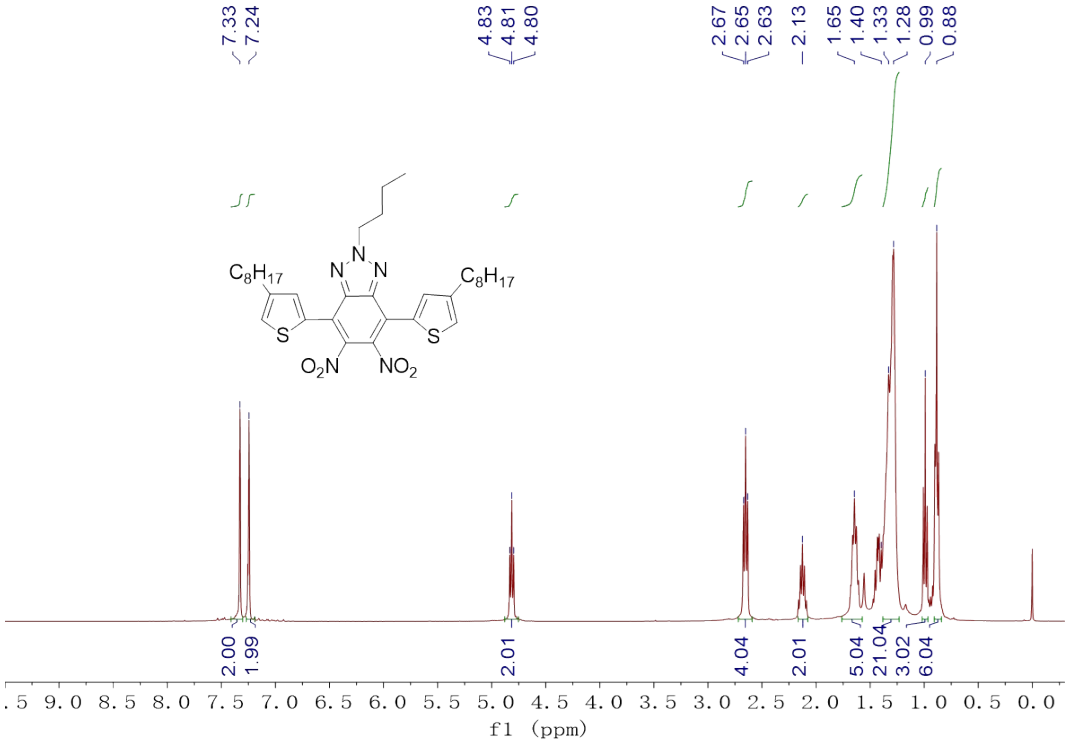

Figure S1. ^{1}H NMR spectrum of compound 3.

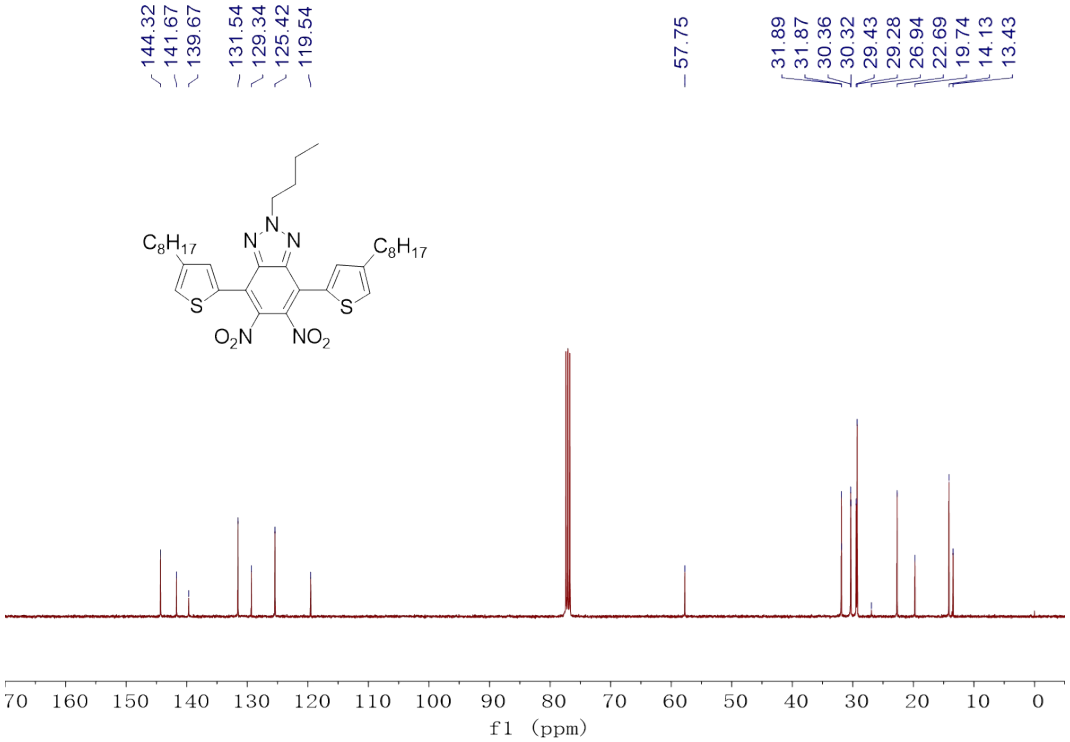

Figure S2. ^{13}C NMR spectrum of compound 3.

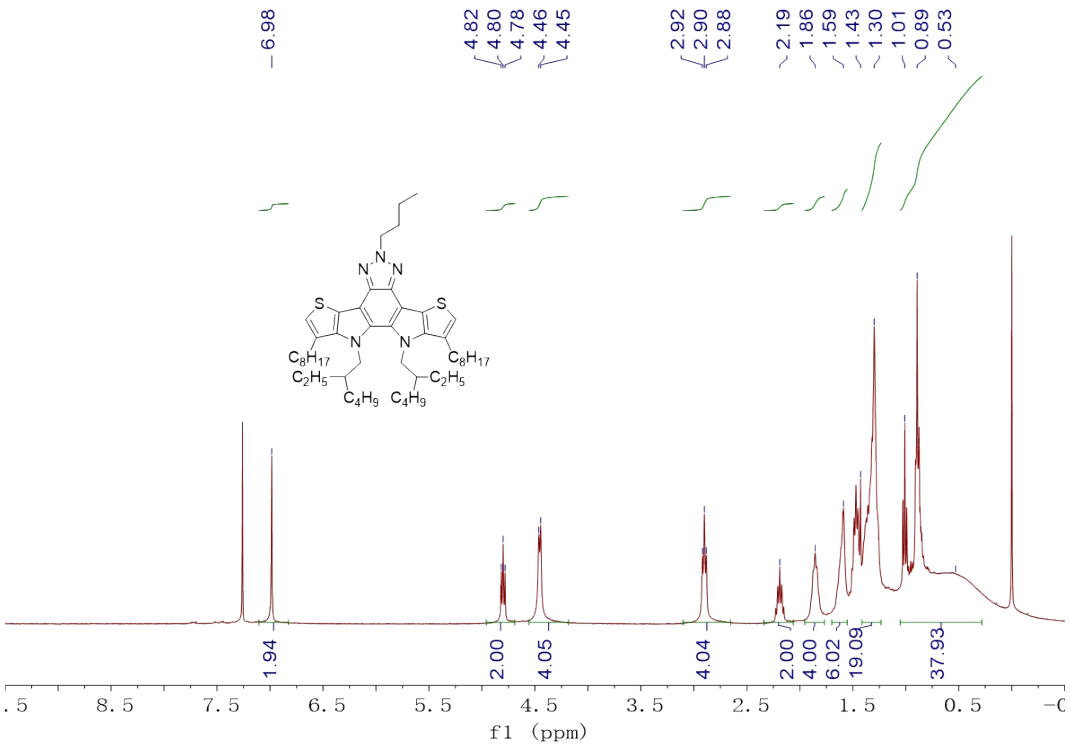

Figure S3. ^{1}H NMR spectrum of compound 4.

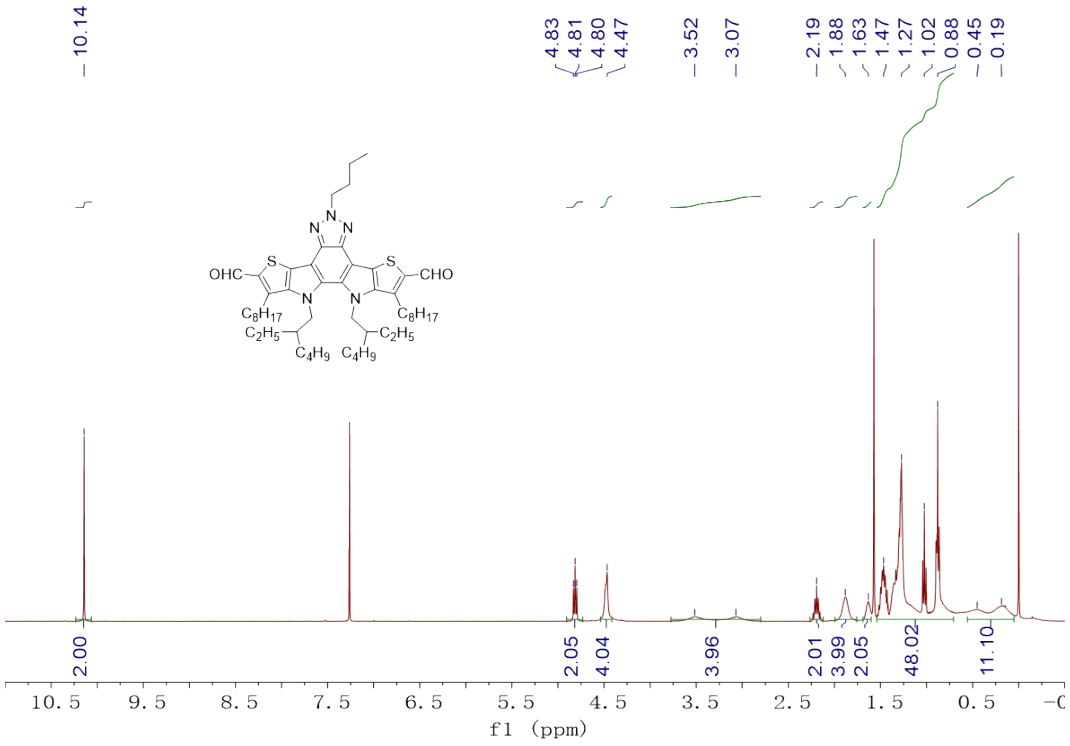

Figure S4. ^{1}H NMR spectrum of compound 5.

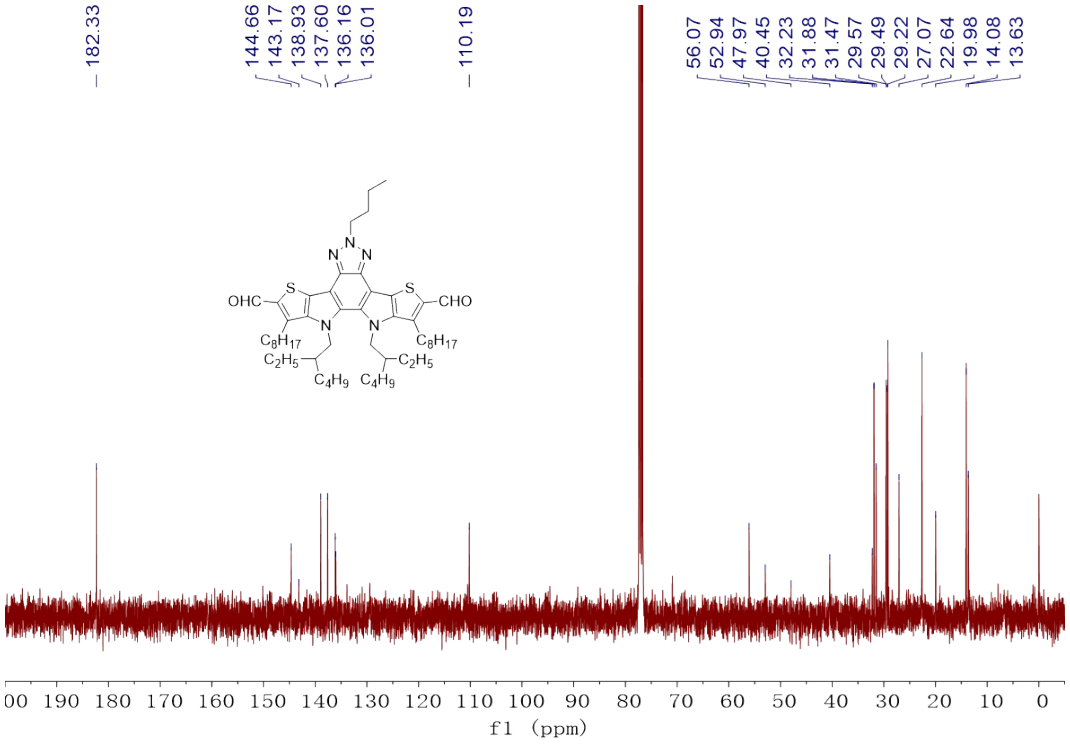

Figure S5. ^{13}C NMR spectrum of compound 5.

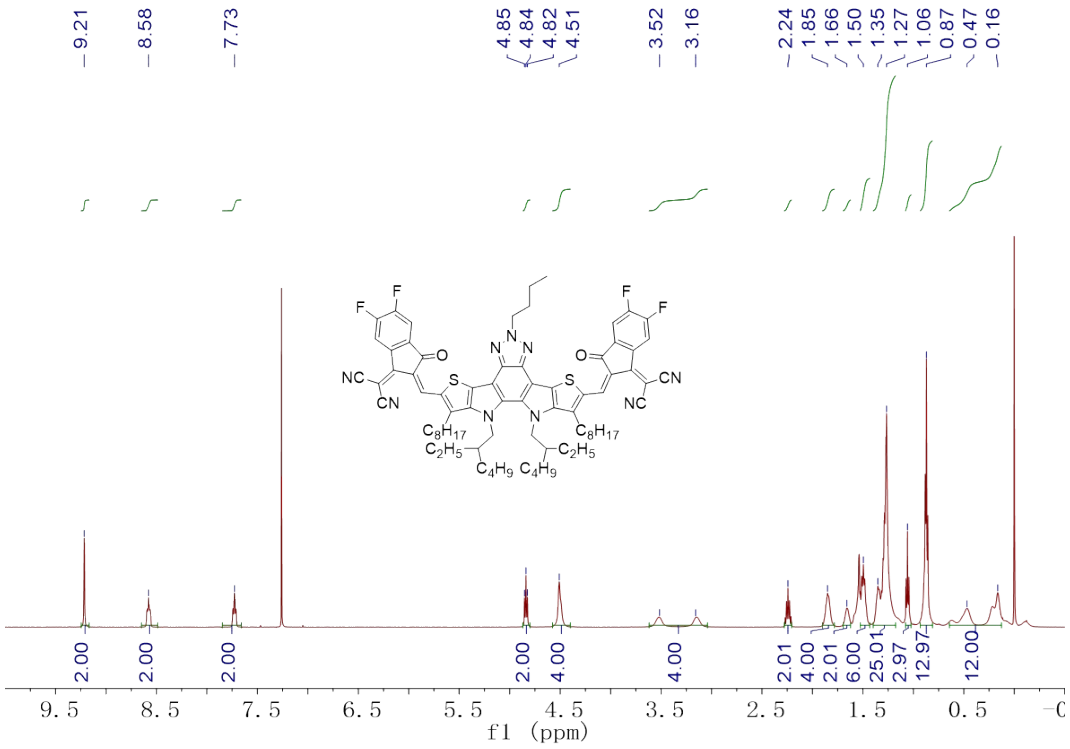

Figure S6. ^{1}H NMR spectrum of compound BTA-C4-F.

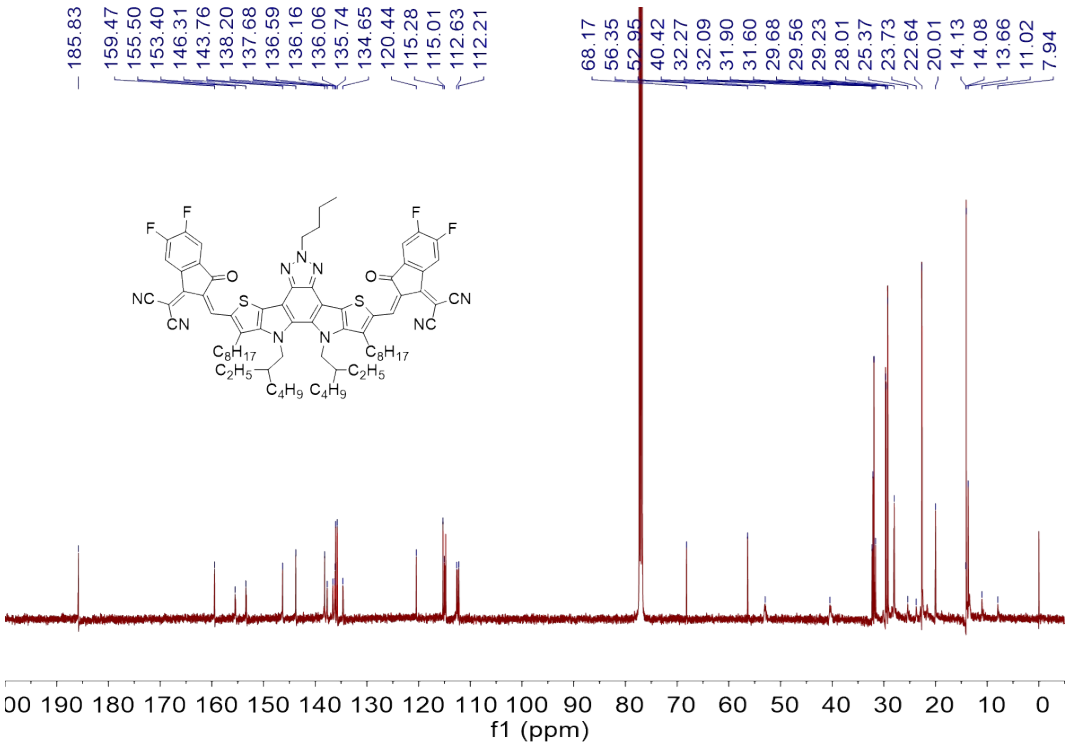

Figure S7. ^{13}C NMR spectrum of compound BTA-C4-F.

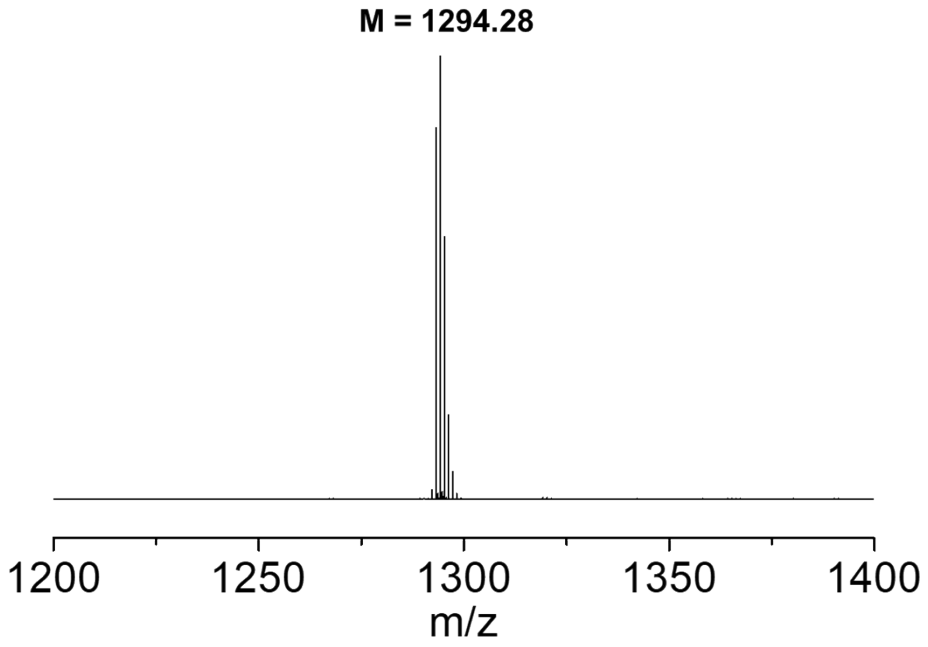

Figure S8. MALDI-TOF mass spectrum of BTA-C4-F.

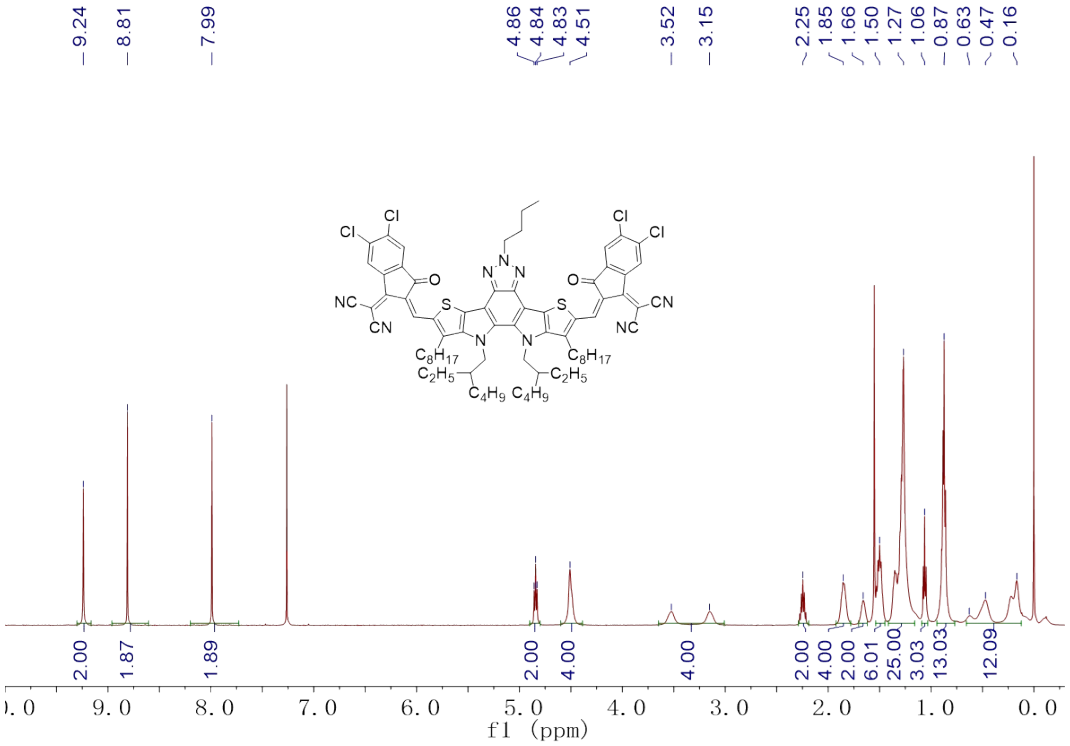

Figure S9. ^{1}H NMR spectrum of compound BTA-C4-Cl.

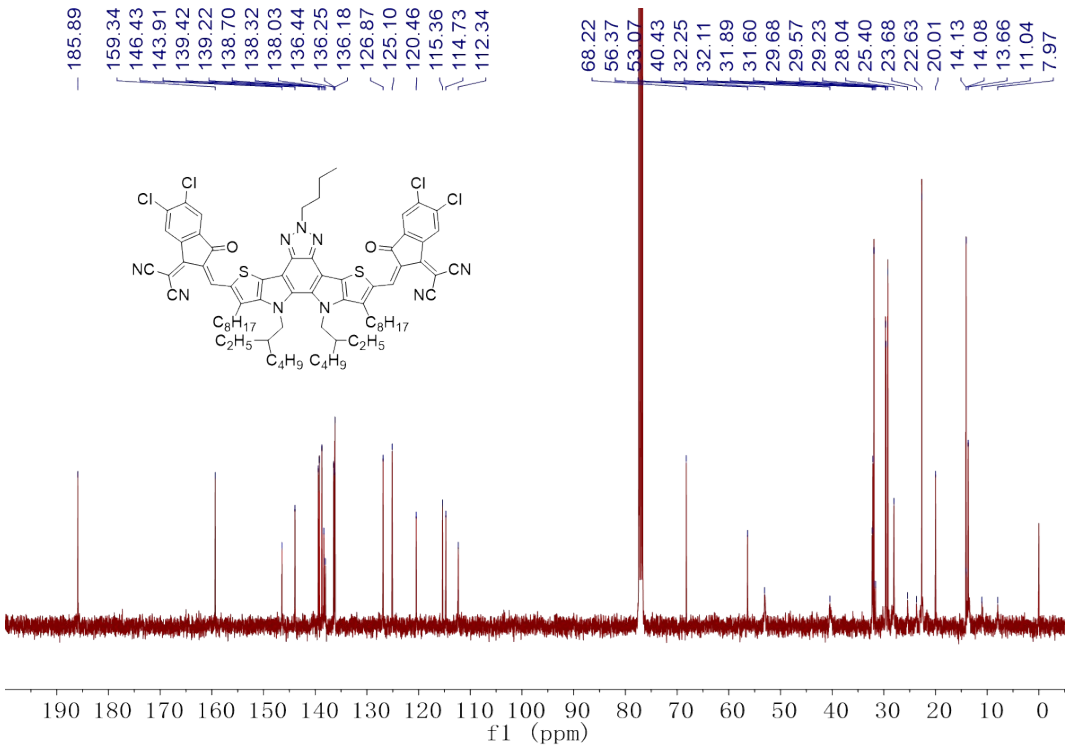

Figure S10. ^{13}C NMR spectrum of compound BTA-C4-Cl.

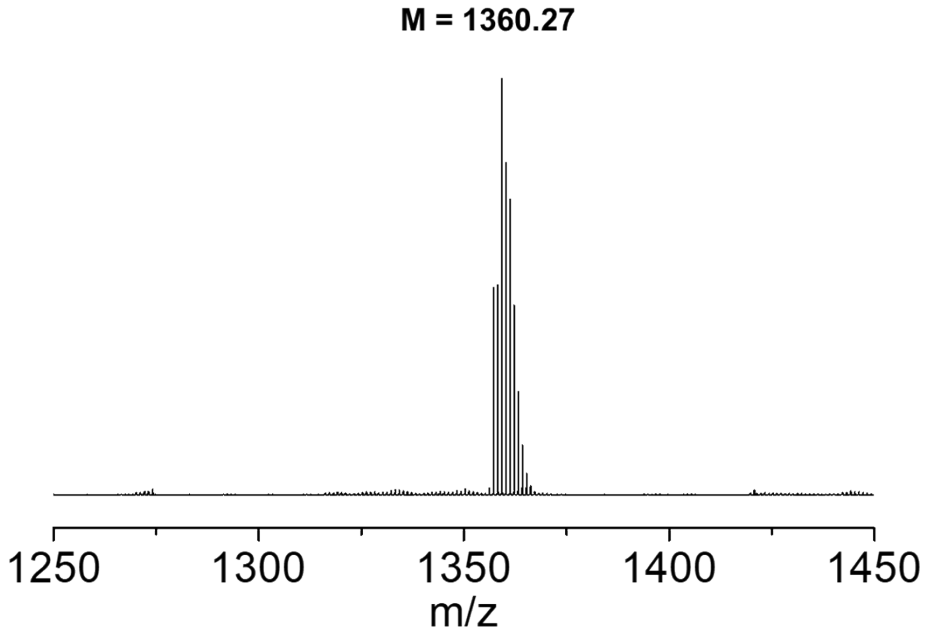

Figure S11. MALDI-TOF mass spectrum of BTA-C4-Cl.

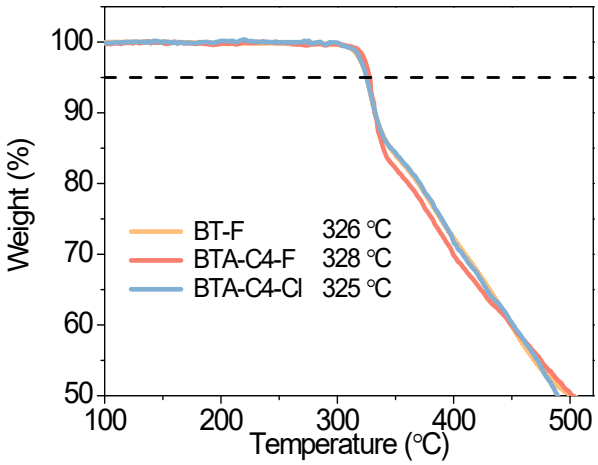

Figure S12. TGA curves of BT-F, BTA-C4-F, and BTA-C4-Cl.

Table S1. Thermal and optical properties of BT-F, BTA-C4-F, and BTA-C4-Cl.

Acceptor	T_d (°C)	λ_{max}^{sol} (nm)	λ_{onset}^{sol} (nm)	λ_{max}^{film} (nm)	λ_{onset}^{film} (nm)	E_g^{opt} a) (eV)
BT-F	326	704	739	770	817	1.52
BTA-C4-F	328	724	762	791	845	1.47
BTA-C4-Cl	325	739	775	809	861	1.44

a) E_g^{opt} is calculated from the onset of the absorption spectrum of neat film.

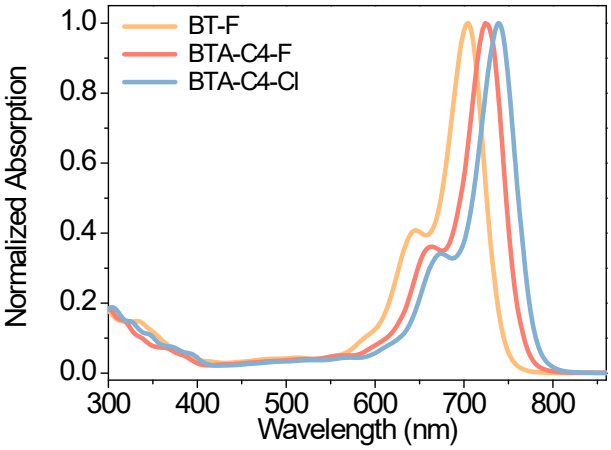

Figure S13. Absorption spectra of BT-F, BTA-C4-F, and BTA-C4-Cl in dilute chloroform solutions.

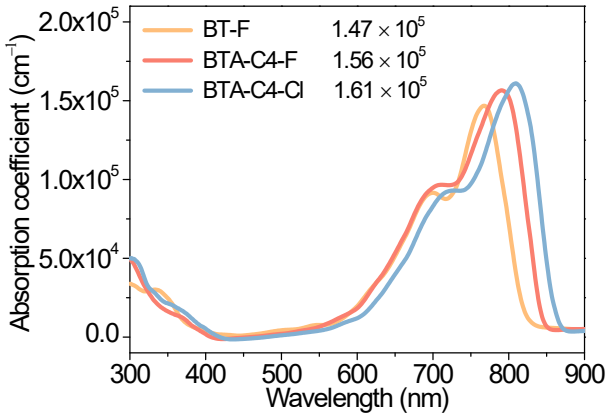

Figure S14. Absorption coefficient spectra of BT-F, BTA-C4-F, and BTA-C4-Cl neat films.

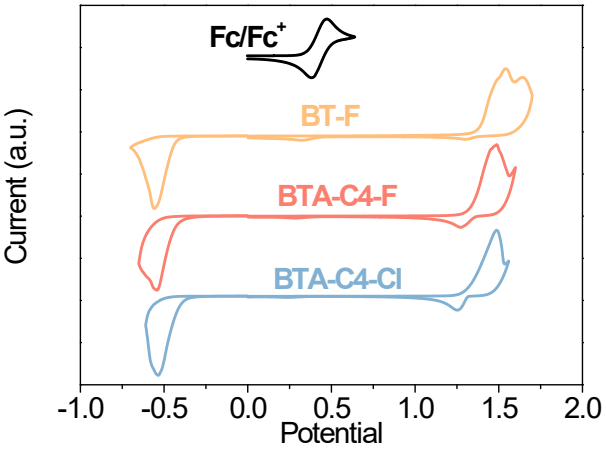

Figure S15. Cyclic voltammograms of ferrocene/ferrocenium (Fc/Fc^+) couple, BT-F, BTA-C4-F, and BTA-C4-Cl.

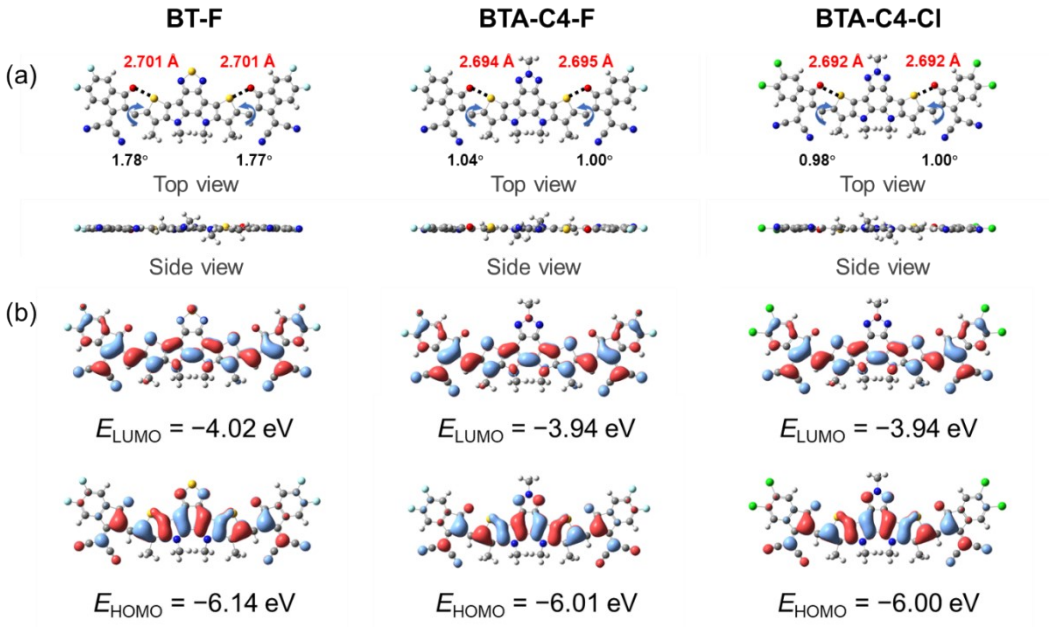

Figure S16. (a) Top view and side view of the optimized structure, (b) charge density distribution and the calculated energy levels of BT-F, BTA-C4-F, and BTA-C4-Cl.

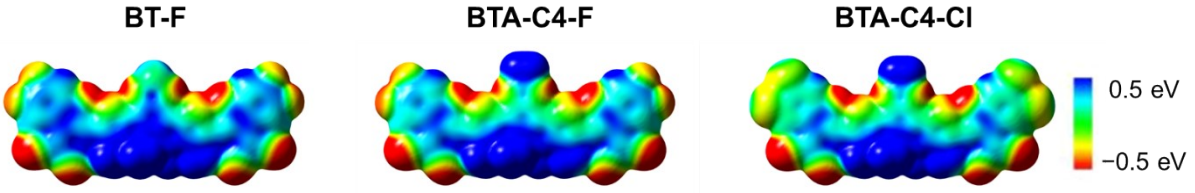

Figure S17. ESP distribution of BT-F, BTA-C4-F, and BTA-C4-Cl.

Table S2. Ground- and excited-state dipole moments in the x, y, and z direction of BT-F, BTA-C4-F, and BTA-C4-Cl.

Acceptor	μ_{gx}	μ_{gy}	μ_{gz}	μ_{ex}	μ_{ey}	μ_{ez}	$\Delta\mu_{ge}$
BT-F	−0.0001	0.7693	0.0001	8.5619	−0.0001	−0.0384	8.597
BTA-C4-F	−0.0011	0.4527	0.0198	−8.7639	0.0002	−0.0012	8.775
BTA-C4-Cl	−0.0010	0.6651	0.0200	−8.8138	0.0003	0.0091	8.838

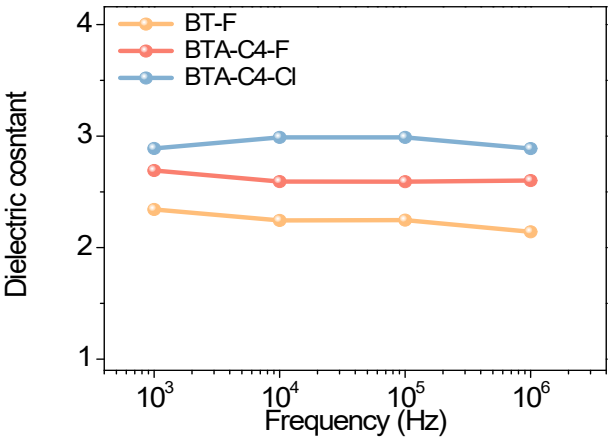

Figure S18. Relative dielectric constants of BT-F, BTA-C4-F, and BTA-C4-Cl.

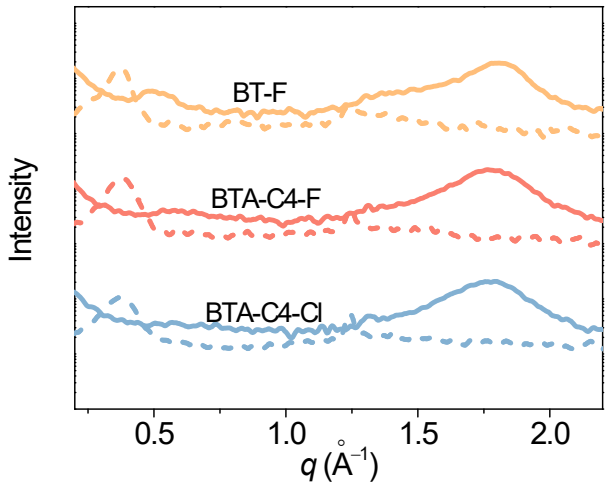

Figure S19. One-dimensional GIWAXS profiles of neat films of BT-F, BTA-C4-F, and BTA-C4-Cl. For the line-cut profiles, solid line depicts out-of-plane and dash line depicts in-plane.

Table S3. GIWAXS parameters of the neat films of BT-F, BTA-C4-F, and BTA-C4-Cl.

Sample	OOP (010)			IP (100)		
	q (Å^{-1})	*d*-spacing (Å)	CCL (Å)	*q* (Å^{-1})	*d*-spacing (Å)	CCL (Å)
BT-F	1.80	3.49	25.69	0.38	16.53	75.54
BTA-C4-F	1.77	3.55	26.16	0.38	16.53	63.28
BTA-C4-Cl	1.80	3.49	26.32	0.38	16.53	46.81

Table S4. Crystal data and structure refinements for BT-F[a)], BTA-C4-F, and BTA-C4-Cl.

Identification code	BT-F	BTA-C4-F	BTA-C4-Cl
Empirical formula	$C_{80}H_{90}F_4N_8O_2S_3$	$C_{76}H_{78}F_4N_9O_2S_2$	$C_{71}H_{52}Cl_4N_9O_2S_2$
Formula weight	1367.77	1289.59	3979.76
Temperature (K)	150.00 (10)	150.00 (10)	293.00 (10)
Wavelength (Å)	1.54184	1.54184	1.54184
Crystal system	monoclinic	Triclinic	monoclinic
Space group	*C2/c*	*P*-1	*I2/a*
a (Å)	30.7548 (11)	14.9787 (7)	20.0971 (2)
b (Å)	10.0625 (3)	15.6453 (7)	24.3131 (2)
c (Å)	29.1709 (8)	15.6646 (11)	56.2506 (5)
α (°)	90	85.291 (4)	90
β (°)	108.356 (4)	68.991 (5)	90.019 (1)
γ (°)	90	81.688 (4)	90
V (Å^3)	8568.2 (5)	3389.1 (3)	27485.3 (4)
Z	4	2	4
Density(calculated) (g cm^{-3})	1.060	1.264	0.962
Absorption coefficient (mm^{-1})	1.221	1.238	1.914
F (000)	2904.0	1362.0	8284.0
Crystal size (mm^3)	0.07 × 0.06 × 0.05	0.04 × 0.05 × 0.20	0.04 × 0.03 × 0.02
θ range for data collection/°	3.63 to 67.07	2.86 to 74.53	2.85 to 74.17
Index ranges	$-34 \le h \le 36$, $-7 \le k \le 12$, $-34 \le l \le 32$	$-12 \le h \le 16$, $-19 \le k \le 19$, $-18 \le l \le 19$	$-24 \le h \le 24$, $-30 \le k \le 30$, $-41 \le l \le 65$
Reflections collected	20754	33559	149382
Independent reflections	7597 [*R*(int) = 0.051]	13113 [*R*(int) =0.044]	26978 [*R*(int) = 0.039]
Completeness to *θ* = 25.25°	99.3%	94.4%	96.4%
Max. and min. transmission	1.000 and 0.707	1.000 and 0.957	1.000 and 0.822
Data / restraints / parameters	7597 / 42 / 486	13113 / 0 / 844	26978 / 127 / 1246
Goodness-of-fit on F^2	1.054	1.103	1.482
Final *R* indices [*I* > 2sigma(*I*)]	R_1 = 0.0880, wR_2 = 0.2478	R_1 = 0.1982, wR_2 = 0.6373	R_1 = 0.1067, wR_2 = 0.3237
R indices (all data)	R_1 = 0.0959, wR_2 = 0.2569	R_1 = 0.2217, wR_2 = 0.6754	R_1 = 0.1299, wR_2 = 0.3578
Largest diff. peak and hole (e·Å^{-3})	0.51 and −0.56	1.86 and −0.72	1.27 and −0.86

[a)] The crystal data of BT-F has been published in our previous work, namely BTPT4F-BO (CCDC: 2290409)[3].

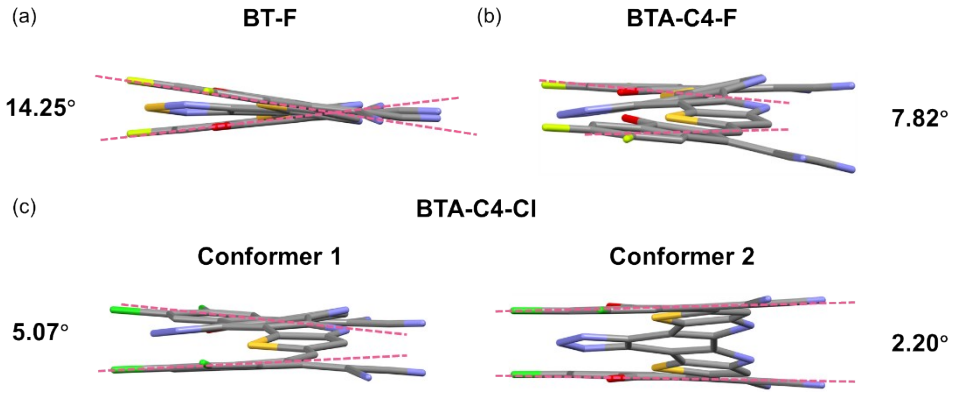

Figure S20. Torsion angles consisting of planes built from the two end groups of (a) BT-F, (b) BTA-C4-F, and (c) BTA-C4-Cl.

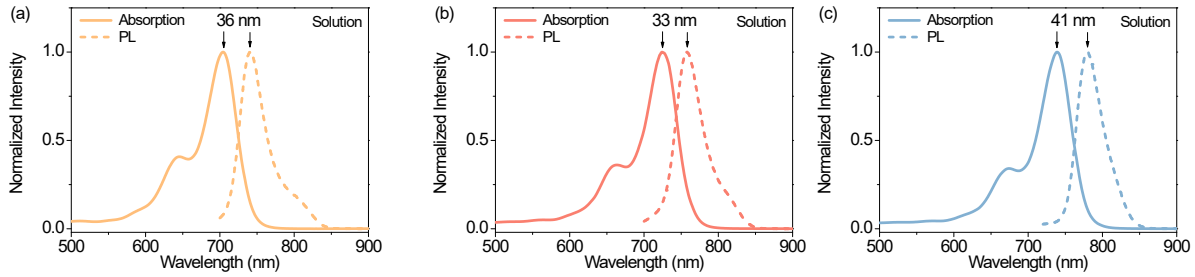

Figure S21. Normalized UV–*vis*–NIR absorption and photoluminescence (PL) spectra of (a) BT-F, (b) BTA-C4-F, and (c) BTA-C4-Cl in dilute chloroform solution.

Table S5. Stokes shifts of BT-F, BTA-C4-F, BTA-C4-Cl, and Y6[9] in solutions.

Acceptor	Solution Stokes shift (nm)
BT-F	36
BTA-C4-F	33
BTA-C4-Cl	41
Y6	66

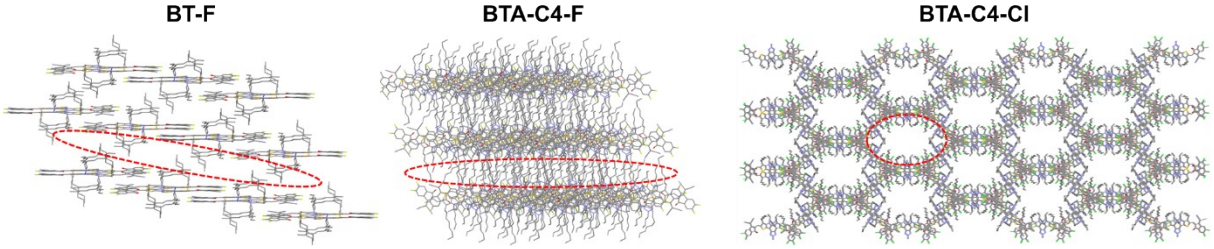

Figure S22. The lamellar stacking among alkyl chains of BT-F, BTA-C4-F, and BTA-C4-Cl.

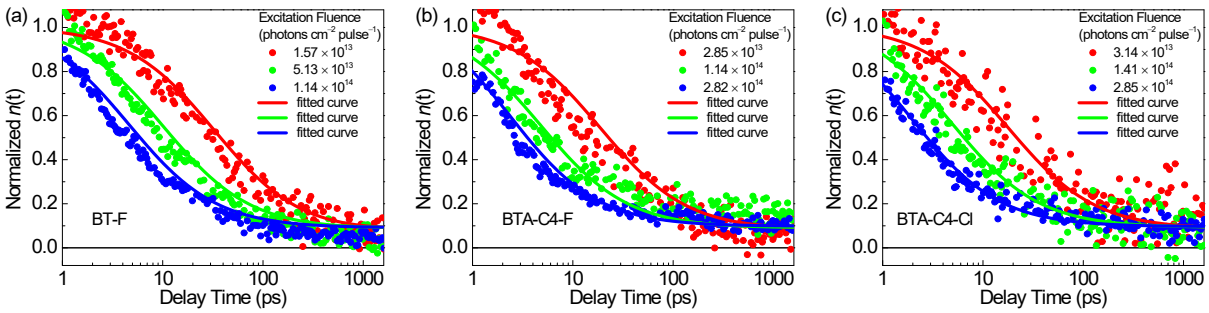

Figure S23. Exciton diffusion length measurements of (a) BT-F, (b) BTA-C4-F, and (c) BTA-C4-Cl. The fluence dependent singlet-exciton decays are fitted to the exciton-exciton annihilation model.

Table S6. The parameters for exciton diffusion length measurements.

Neat film	τ (ps)	γ (cm^3·s^{-1})	D (cm^2·s^{-1})	L_d (nm)	Probe (nm)
BT-F	526	4.14 × 10^{-8}	1.65 × 10^{-2}	51.02	770
BTA-C4-F	594	4.02 × 10^{-8}	1.59 × 10^{-2}	53.41	805
BTA-C4-Cl	934	3.43 × 10^{-8}	1.36 × 10^{-2}	61.84	805

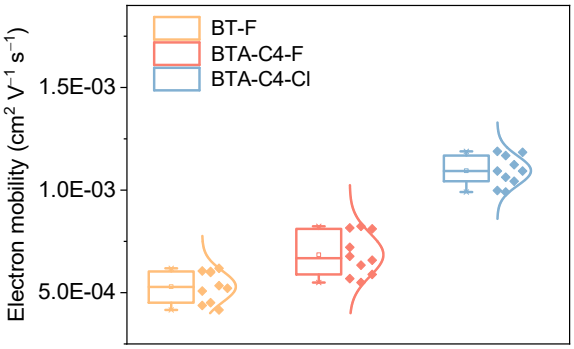

Figure S24. Electron mobilities obtained from single-carrier devices based on neat film of BT-F, BTA-C4-F, and BTA-C4-Cl.

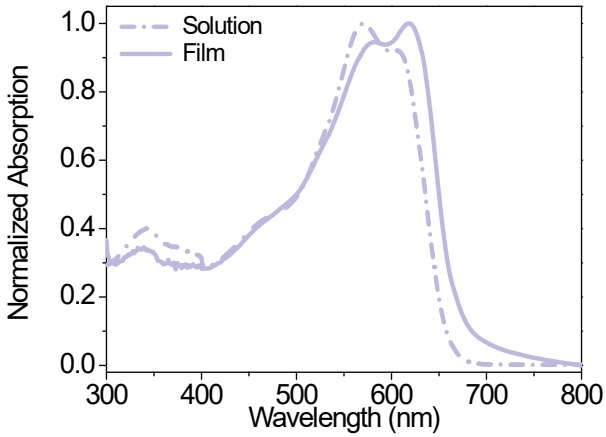

Figure S25. Absorption spectra of PBDCT in chloroform solution and neat film.

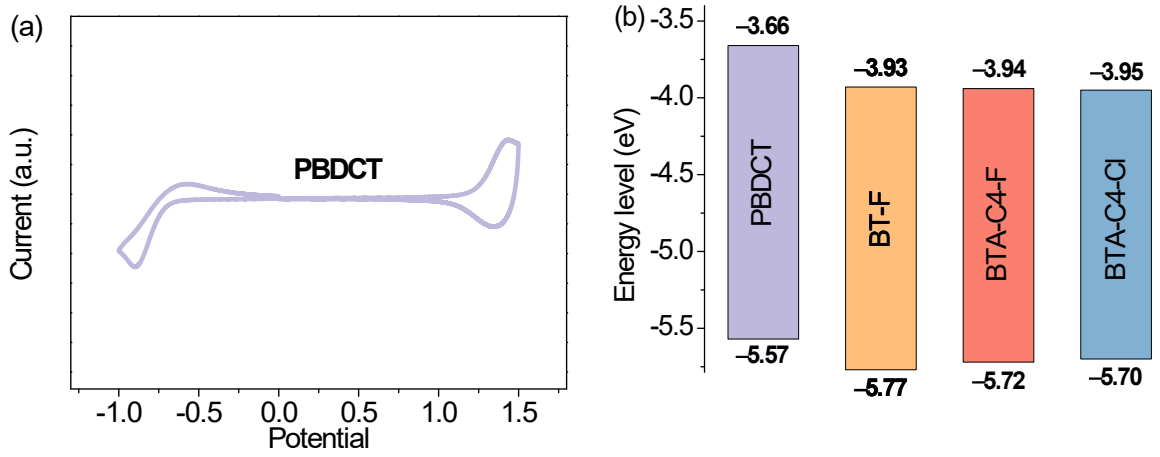

Figure S26. (a) Cyclic voltammogram of PBDCT. (b) Energy level diagrams of PBDCT, BT-F, BTA-C4-F, and BTA-C4-Cl.

Table S7. The device parameters of the OSCs based on BT-F under AM1.5G irradiation at 100 mW cm^{-2}. (DIO is 1,8-diiodooctane; MN is 1-methylnaphthalene; DIB is 1,4-diiodobenzene; DBCB is 1,3-dibromo-5-chlorobenzene)

D:A ratio [*w*/*w*]	Solvent [*v*/*v*]	Annealing [°C]	V_{oc} [V]	J_{sc} [mA cm^{-2}]	FF	PCE [%]
1:1	CF	120	0.899	21.51	71.85	13.89
1:1.2			0.901	21.48	71.07	13.75
1:1.5			0.893	21.36	70.87	13.52
1:1	CF	w/o	0.930	19.64	73.37	13.40
		100	0.916	20.44	74.49	13.95
		120	0.885	20.13	75.25	13.40
1:1	CF	100	0.916	20.44	74.49	13.95
	CF + 0.50% DIO		0.921	19.58	66.44	11.98
	CF + 0.45% MN		0.912	20.56	73.61	13.80
	CF + 5 mg/ml DIB		0.913	21.75	72.64	14.42
	CF + 5 mg/ml DBCB		0.913	21.95	73.53	14.74
1:1	CF + 2 mg/ml DBCB	100	0.913	22.28	72.37	14.72
	CF + 5 mg/ml DBCB		0.914	22.09	73.97	14.93
	CF + 10 mg/ml DBCB		0.914	21.97	73.89	14.83

Table S8. The device parameters of the OSCs based on BTA-C4-F under AM 1.5G irradiation at 100 mW cm^{-2}.

D:A ratio [*w*/*w*]	Solvent [*v*/*v*]	Annealing [°C]	V_{oc} [V]	J_{sc} [mA cm^{-2}]	FF	PCE [%]
1:1	CF	100	0.901	22.61	74.53	15.18
1:1.2			0.902	22.48	73.19	14.84
1:1.5			0.899	22.13	73.73	14.66
1:1	CF	w/o	0.913	21.47	71.67	14.05
		100	0.901	22.26	72.09	14.46
		120	0.893	22.05	73.41	14.45
1:1	CF	100	0.903	22.40	74.89	15.15
	CF + 0.50% DIO		0.902	21.05	71.83	13.64
	CF + 0.45% MN		0.897	22.24	73.34	14.63
	CF + 5 mg/ml DIB		0.898	23.37	73.83	15.49
	CF + 5 mg/ml DBCB		0.907	23.50	74.51	15.90
1:1	CF + 2 mg/ml DBCB	100	0.911	23.19	71.43	15.09
	CF + 5 mg/ml DBCB		0.907	23.50	74.51	15.90
	CF + 10 mg/ml DBCB		0.901	23.43	73.39	15.49

Table S9. The device parameters of the OSCs based on BTA-C4-Cl under AM 1.5G irradiation at 100 mW cm^{-2}.

D:A ratio [*w*/*w*]	Solvent [*v*/*v*]	Annealing [°C]	V_{oc} [V]	J_{sc} [mA cm^{-2}]	FF	PCE [%]
1:1			0.885	22.97	73.74	14.99
1:1.2	CF	100	0.889	22.51	73.86	14.78
1:1.5			0.886	21.61	74.58	14.28
		w/o	0.886	21.03	73.10	13.62
1:1	CF	100	0.881	23.28	71.53	14.67
		120	0.863	23.81	69.45	14.27
	CF		0.885	22.14	73.49	14.40
	CF + 0.50% DIO		0.892	24.31	72.75	15.77
1:1	CF + 0.45% MN	100	0.890	24.82	73.44	16.22
	CF + 5 mg/ml DIB		0.891	24.83	74.58	16.51
	CF + 5 mg/ml DBCB		0.893	25.23	74.00	16.67
	CF + 2 mg/ml DBCB		0.899	25.02	74.25	16.69
1:1	CF + 5 mg/ml DBCB	100	0.893	25.51	74.72	17.01
	CF + 7.5 mg/ml DBCB		0.894	25.52	75.26	17.16

Table S10. Photovoltaic parameters of OSCs based on A–DA'D–A-type pentacyclic FREAs.

Year	Acceptor	Donor	V_{oc} (V)	J_{sc} (mA cm^{-2})	FF (%)	PCE (%)	Ref.
2024	BTA-C4-Cl	PBDCT	0.894	25.52	75.26	17.16	
2024	BTA-C4-F	PBDCT	0.907	23.50	74.51	15.90	*This work*
2024	BT-F	PBDCT	0.914	22.09	73.97	14.93	
2017	BZIC	HFQx-T	0.84	12.67	59.00	6.30	[10]
2021	Y25	PM6	0.80	20.19	72.14	11.65	[11]
2021	Y26	PM6	0.83	21.63	74.33	13.34	[11]
2022	BZ4F	PM6	0.85	22.53	71.98	13.79	[12]
2022	BZ4F-O-1	PM6	0.91	19.57	75.61	13.50	[12]
2022	BZ4F-O-2	PM6	0.82	21.62	74.74	13.43	[12]
2022	BZ4F-O-3	PM6	0.85	23.51	73.72	14.69	[12]
2022	DPBT-2Cl	PM6	0.78	23.08	64.01	11.5	[13]
2022	Y26	PTQ10	0.886	23.57	76.73	16.01	[14]
2023	BZ4F	PM6	0.842	22.53	75.3	14.25	[15]
2023	BZ4F-EH	PM6	0.880	22.34	75.1	14.67	[15]
2023	BZ4F-OEH	PM6	0.855	24.43	79.3	16.56	[15]
2023	L1-EH	PM6	0.809	20.03	73.0	11.84	[16]
2023	L1-BO	PM6	0.848	20.76	74.4	13.15	[16]
2023	BTPT4F-EH	PBCT-2F	0.92	18.8	67.7	11.7	[3]
2023	BTPT4F-BO	PBCT-2F	0.89	22.0	76.3	15.0	[3]
2023	BTPT4F-HD	PBCT-2F	0.89	19.9	75.1	13.3	[3]

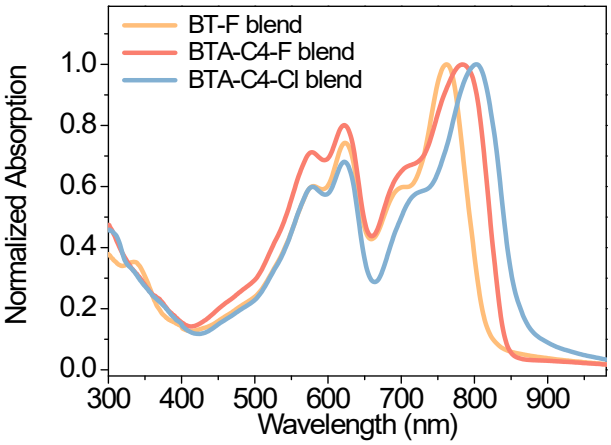

Figure S27. Absorption spectra of the blend films based on BT-F, BTA-C4-F, and BTA-C4-Cl.

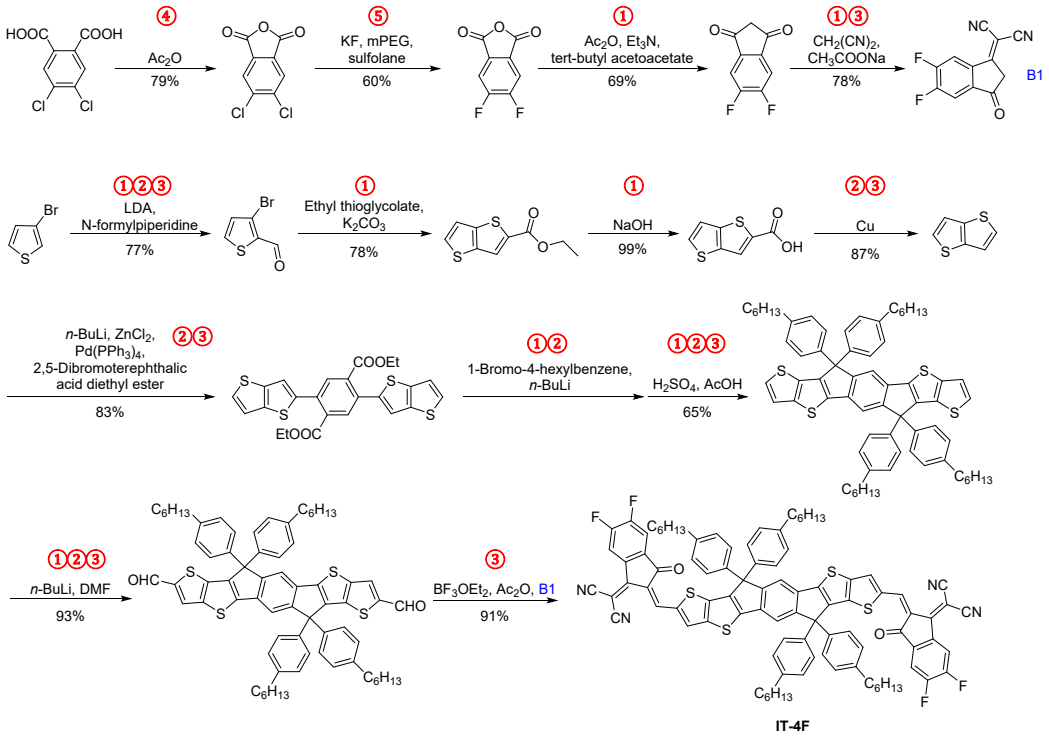

Scheme S2. Synthetic route of IT-4F. The unit operations are represented by codes: 1 = quenching/neutralization, 2 = extraction, 3 = column chromatography, 4 = recrystallization, 5 = distillation/sublimation.

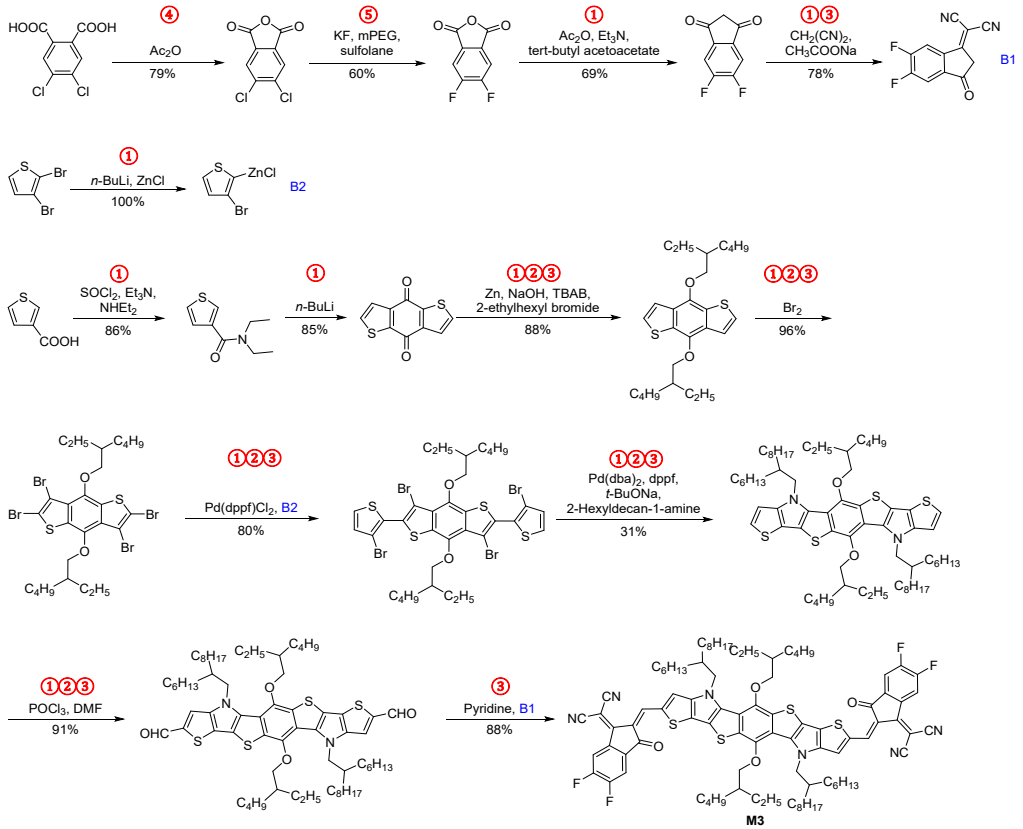

Scheme S3. Synthetic route of M3. The unit operations are represented by codes: 1 = quenching/neutralization, 2 = extraction, 3 = column chromatography, 4 = recrystallization, 5 = distillation/sublimation.

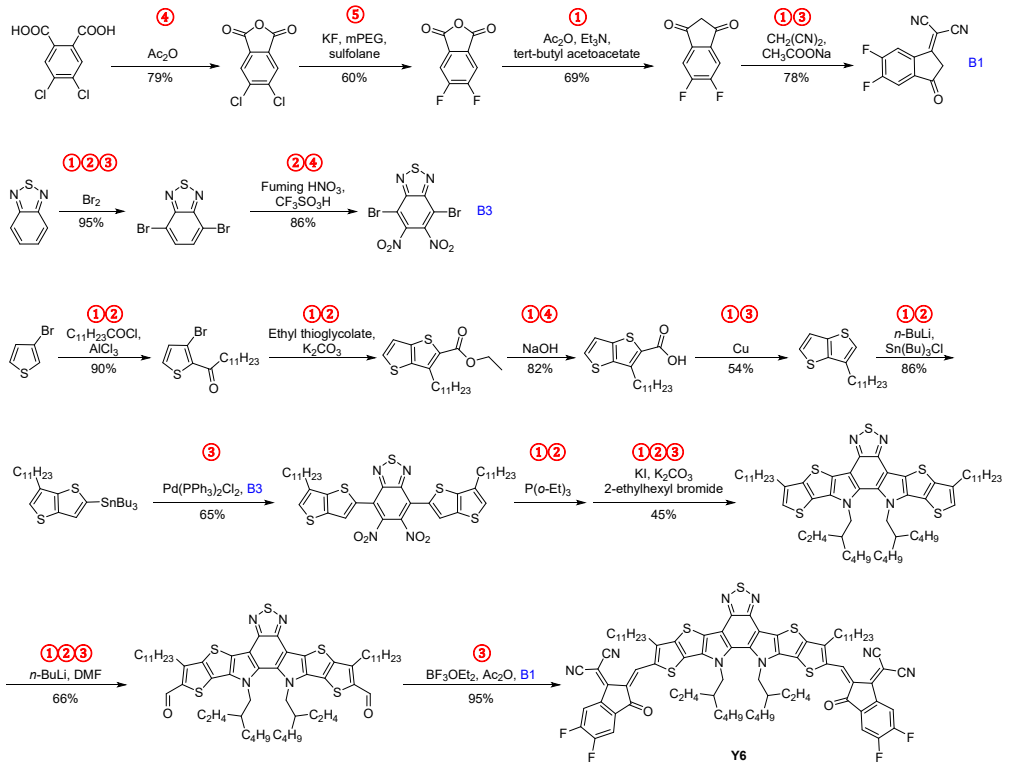

Scheme S4. Synthetic route of Y6. The unit operations are represented by codes: 1 = quenching/neutralization, 2 = extraction, 3 = column chromatography, 4 = recrystallization, 5 = distillation/sublimation.

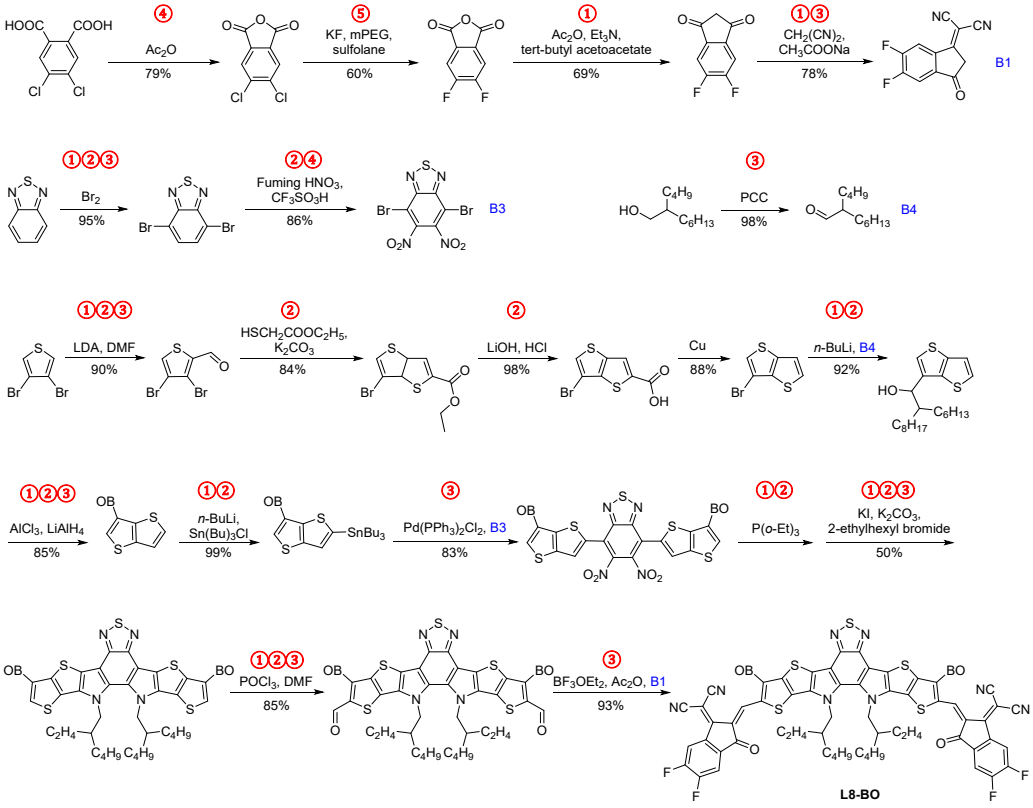

Scheme S5. Synthetic route of L8-BO. The unit operations are represented by codes: 1 = quenching/neutralization, 2 = extraction, 3 = column chromatography, 4 = recrystallization, 5 = distillation/sublimation.

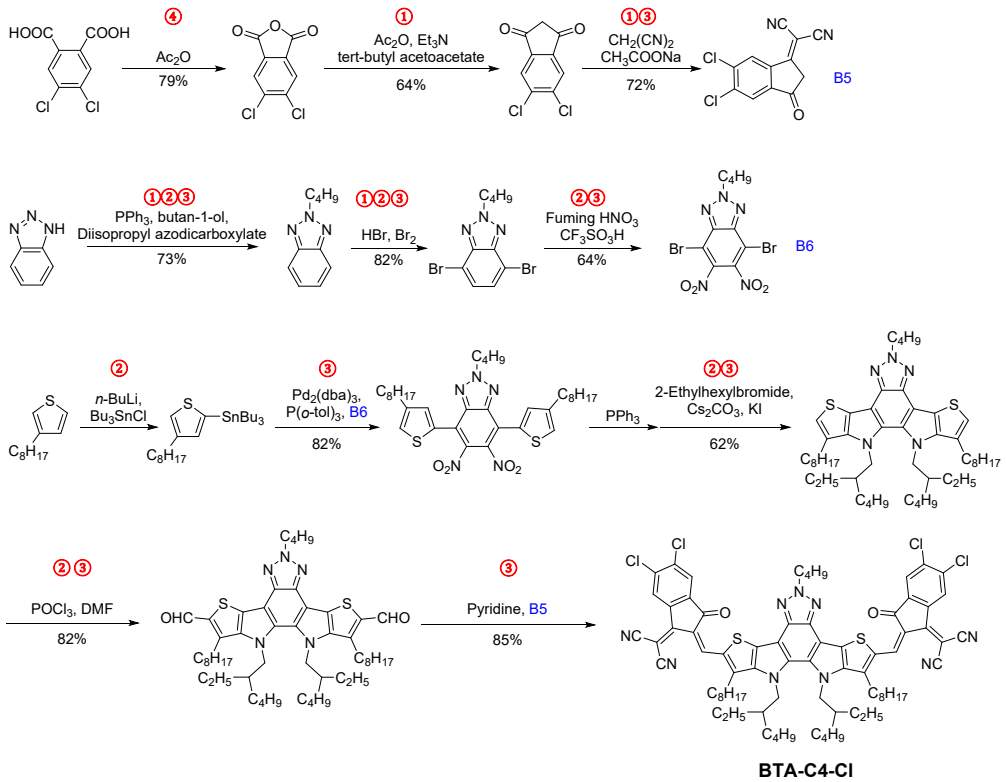

BTA-C4-Cl

Scheme S6. Synthetic route of BTA-C4-Cl. The unit operations are represented by codes: 1 = quenching/neutralization, 2 = extraction, 3 = column chromatography, 4 = recrystallization, 5 = distillation/sublimation.

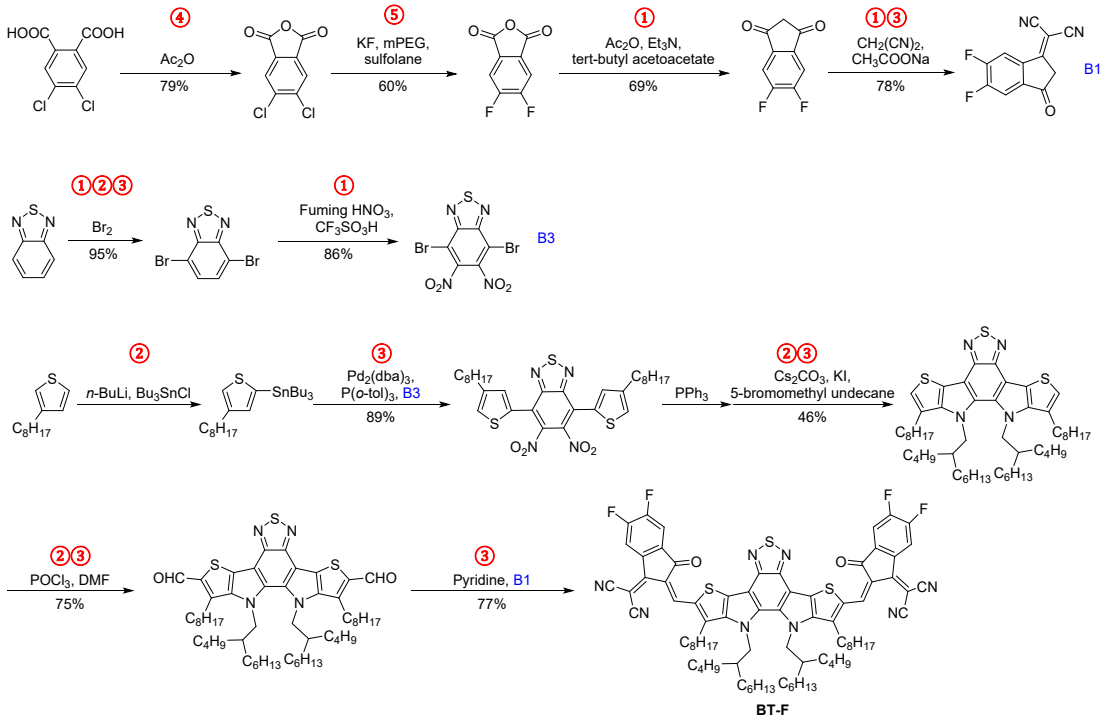

BT-F

Scheme S7. Synthetic route of BT-F. The unit operations are represented by codes: 1 = quenching/neutralization, 2 = extraction, 3 = column chromatography, 4 = recrystallization, 5 = distillation/sublimation.

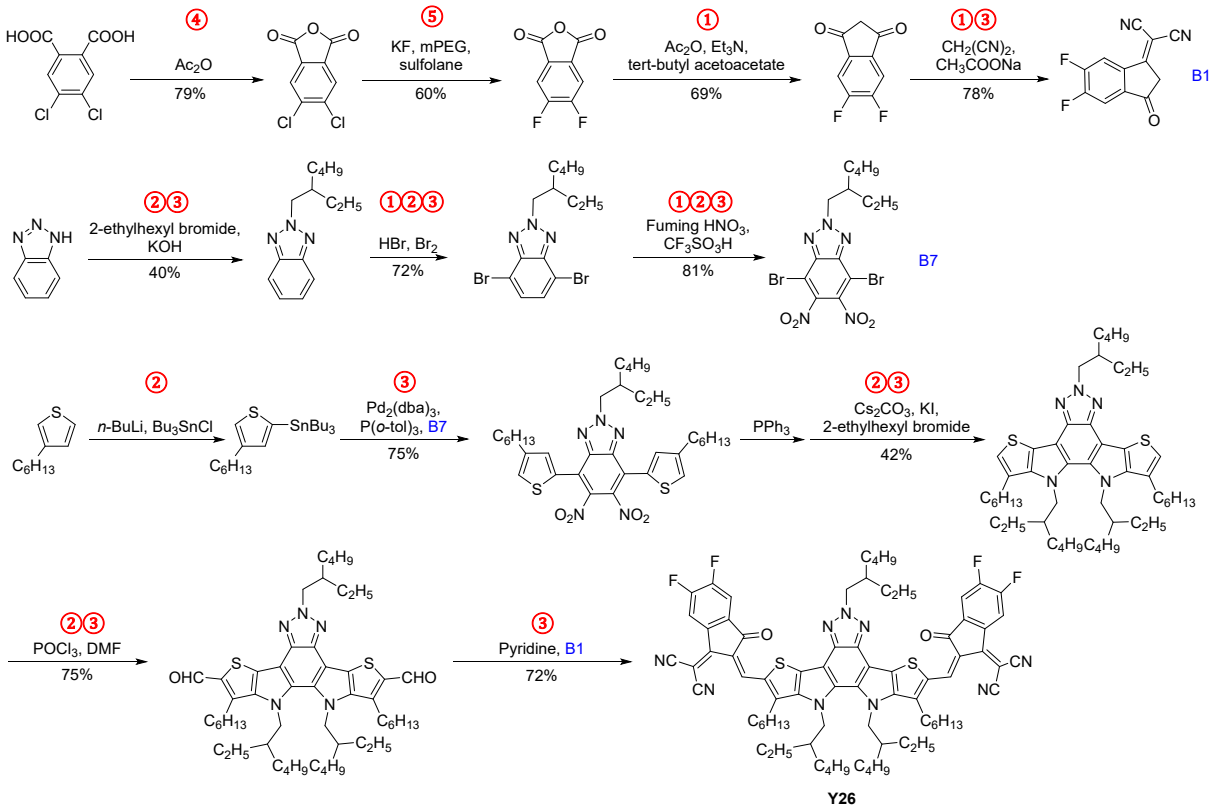

Scheme S8. Synthetic route of Y26. The unit operations are represented by codes: 1 = quenching/neutralization, 2 = extraction, 3 = column chromatography, 4 = recrystallization, 5 = distillation/sublimation.

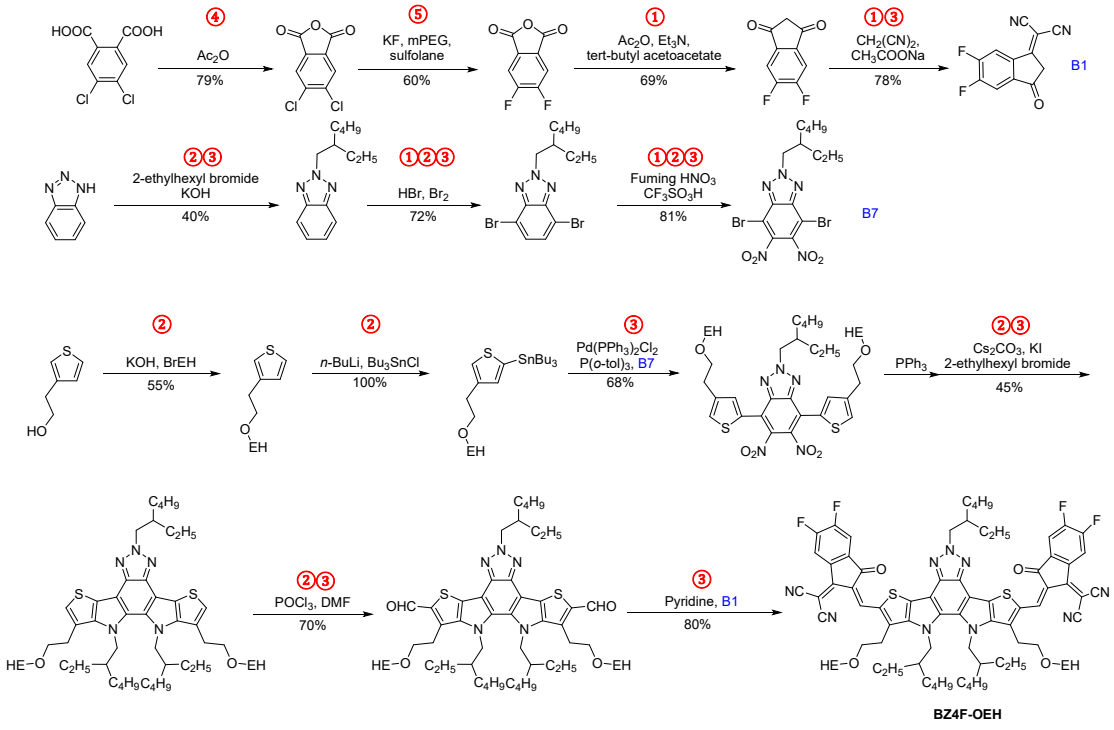

Scheme S9. Synthetic route of BZ4F-OEH. The unit operations are represented by codes: 1 = quenching/neutralization, 2 = extraction, 3 = column chromatography, 4 = recrystallization, 5 = distillation/sublimation.

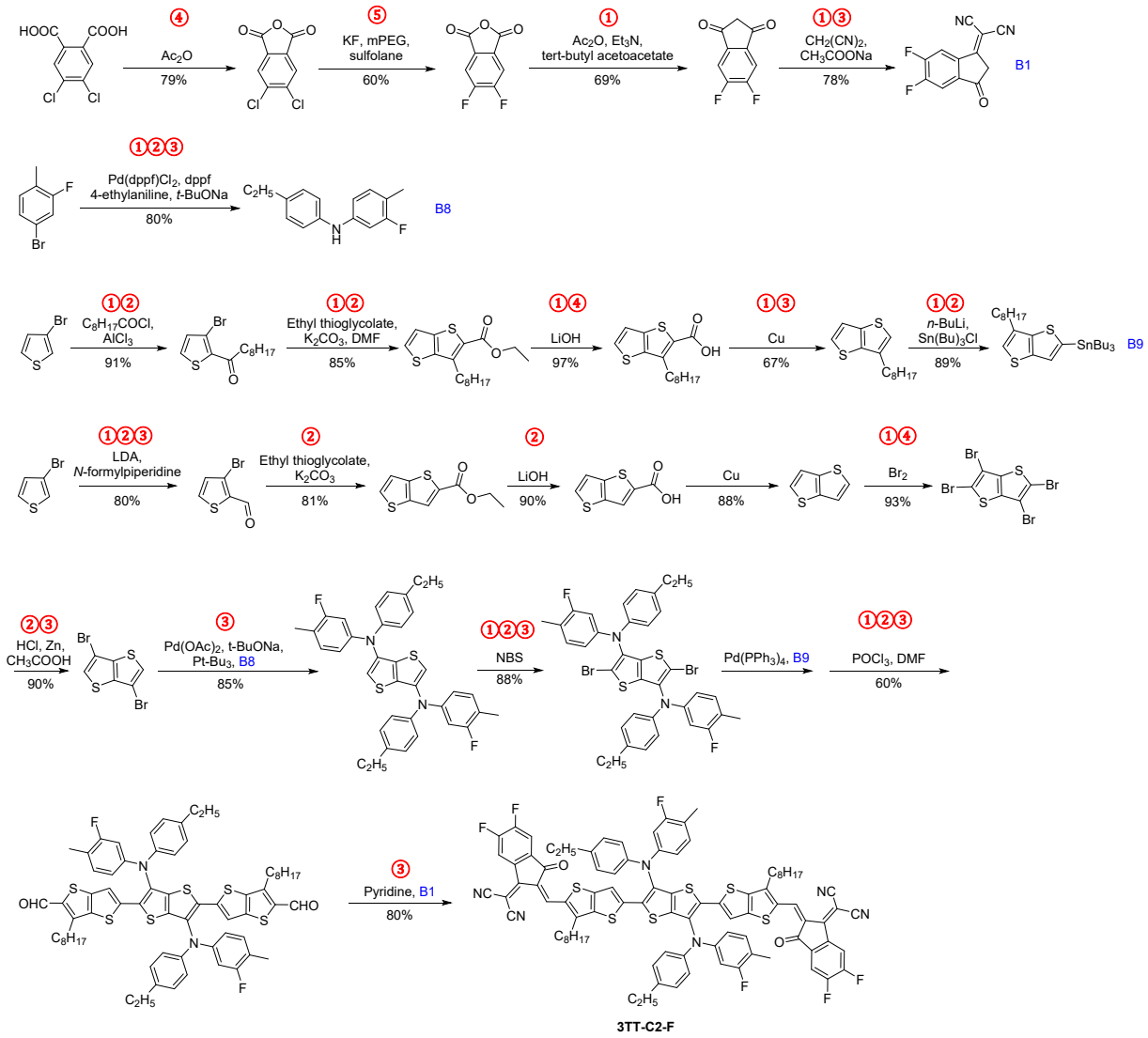

Scheme S10. Synthetic route of 3TT-C2-F. The unit operations are represented by codes: 1 = quenching/neutralization, 2 = extraction, 3 = column chromatography, 4 = recrystallization, 5 = distillation/sublimation.

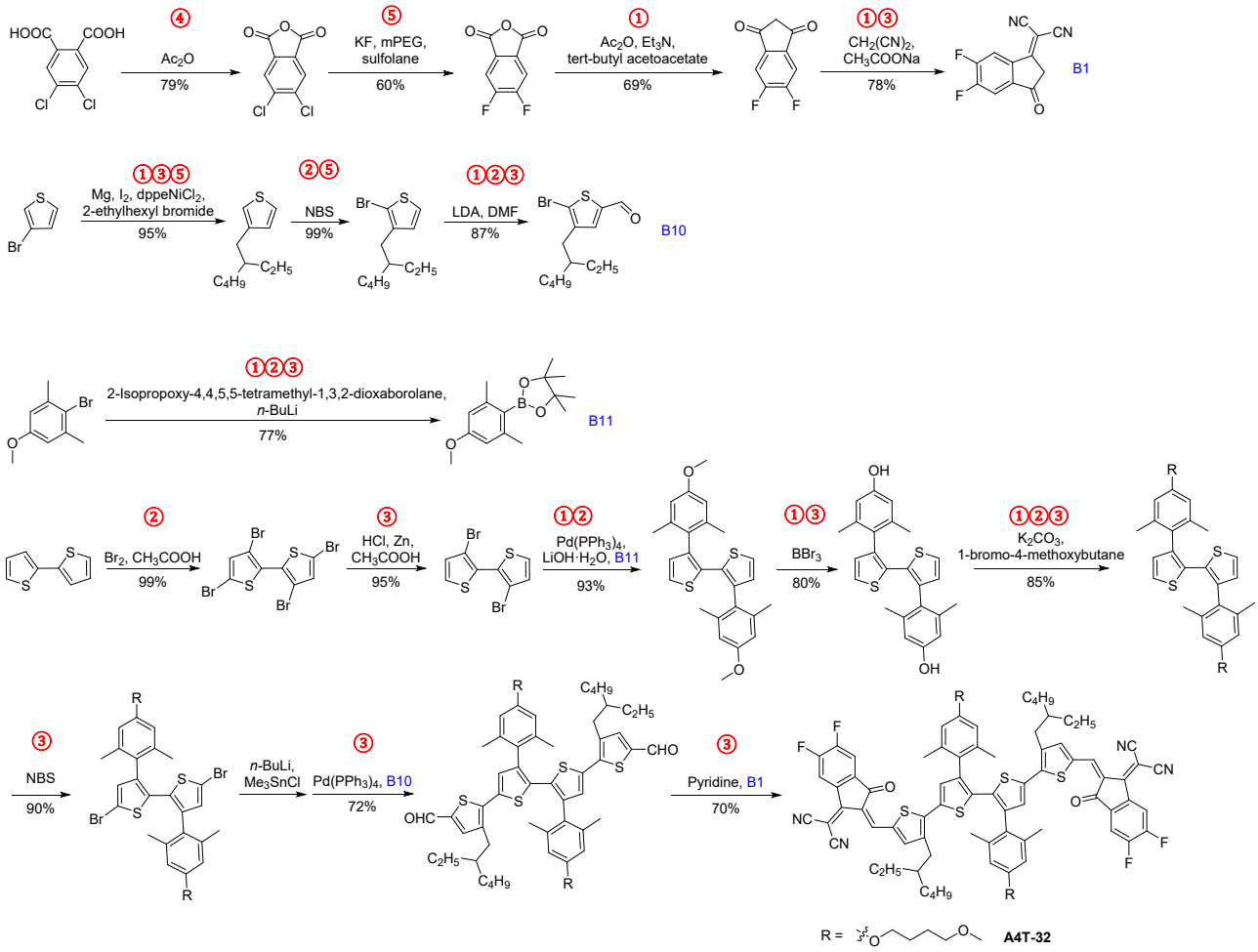

Scheme S11. Synthetic route of A4T-32. The unit operations are represented by codes: 1 = quenching/neutralization, 2 = extraction, 3 = column chromatography, 4 = recrystallization, 5 = distillation/sublimation.

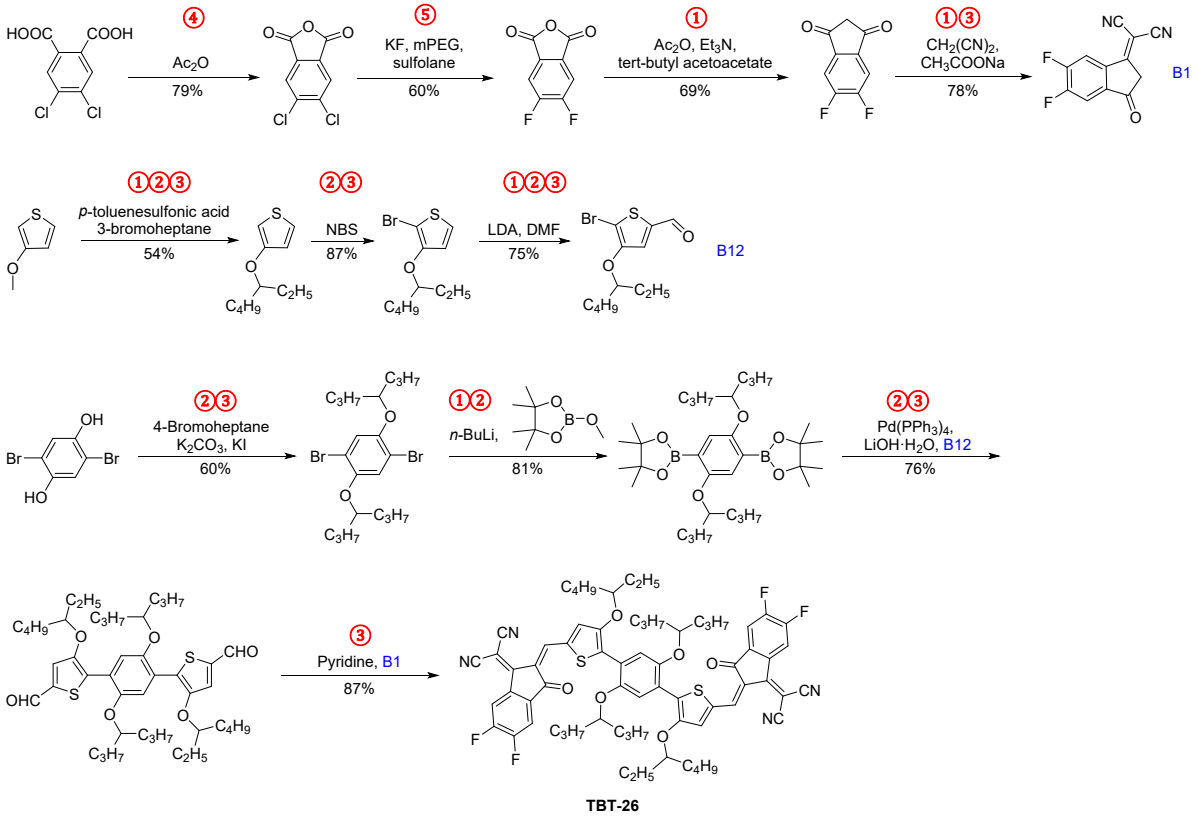

Scheme S12. Synthetic route of TBT-26. The unit operations are represented by codes: 1 = quenching/neutralization, 2 = extraction, 3 = column chromatography, 4 = recrystallization, 5 = distillation/sublimation.

Table S11. The absolute and normalized values of NSS, RY, NUO, NCC, NHC and the SC index of the studied material in this work and state-of-the-art high-performance acceptors in the literatures.

Acceptor	NSS		RY		NUO		NCC		NHC		SC (%)	PCE (%)	FOM	Ref.
	A	N	A	N	A	N	A	N	A	N				
BTA-C4-Cl	12	0.57	2.82	0.40	19	0.54	8	0.80	24	0.69	56.91	17.16	0.302	This work
TBT-26	11	0.52	2.71	0.38	20	0.57	7	0.70	22	0.63	53.21	17.00	0.319	[17]
BT-F	12	0.57	4.23	0.55	16	0.46	6	0.60	23	0.66	56.21	14.99	0.267	[3]
Y26	13	0.62	5.88	0.68	20	0.57	8	0.80	26	0.74	66.59	16.01	0.240	[14]
IT-4F	13	0.62	4.23	0.55	23	0.66	7	0.70	25	0.71	62.96	15.30	0.243	[18-20]
M3	13	0.62	8.15	0.80	24	0.69	7	0.70	26	0.74	69.93	16.70	0.239	[21]
L8-BO	19	0.90	6.10	0.69	33	0.94	9	0.90	32	0.91	85.74	19.60	0.229	[20, 22, 23]
Y6	16	0.76	13.68	1.00	30	0.86	7	0.70	28	0.80	83.02	19.00	0.229	[20, 24, 25]
BZ4F-OEH	14	0.67	10.61	0.90	21	0.60	8	0.80	28	0.80	74.90	16.56	0.221	[15]
A4T-32	17	0.81	3.71	0.50	28	0.80	10	1.00	30	0.86	76.42	15.90	0.208	[26]
3TT-C2-F	21	1.00	8.10	0.80	35	1.00	9	0.90	35	1.00	93.50	17.19	0.184	[27]

Table S12. Charge mobilities of the blends based on BT-F, BTA-C4-F, and BTA-C4-Cl.

Active layer	μ_h (cm^2 V^{-1} s^{-1})	μ_e (cm^2 V^{-1} s^{-1})	μ_h/μ_e
PBDCT:BT-F	3.48×10^{-4}	4.54×10^{-4}	0.77
PBDCT:BTA-C4-F	4.22×10^{-4}	5.24×10^{-4}	0.81
PBDCT:BTA-C4-Cl	5.92×10^{-4}	6.24×10^{-4}	0.95

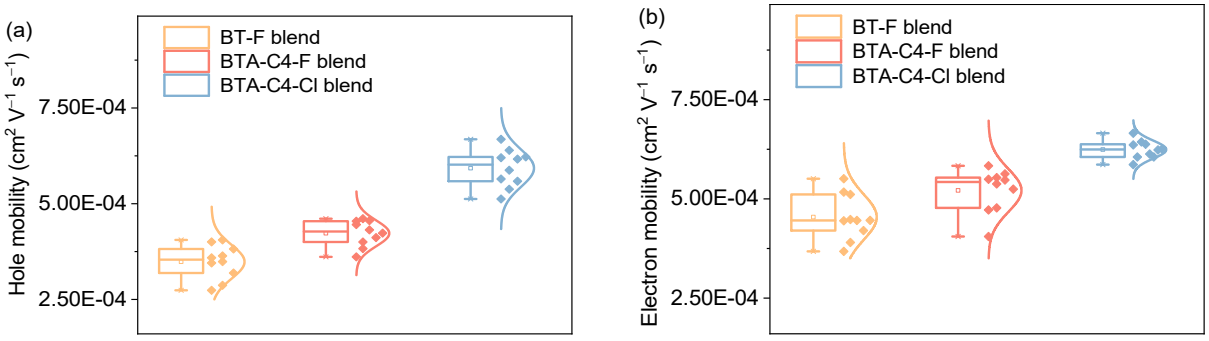

Figure S28. (a) Hole and (b) electron mobilities obtained from single-carrier devices based on blends of BT-F, BTA-C4-F, and BTA-C4-Cl.

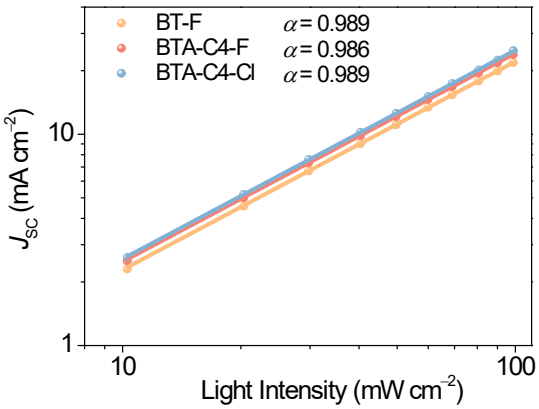

Figure S29. Light intensity dependence of J_{sc} of the optimal OSCs based on BT-F, BTA-C4-F, and BTA-C4-Cl.

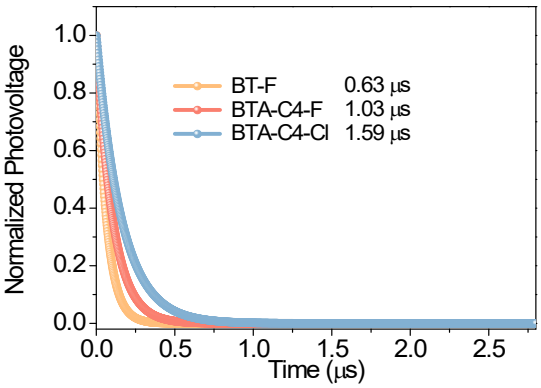

Figure S30. TPV of the optimal OSCs based on BT-F, BTA-C4-F, and BTA-C4-Cl.

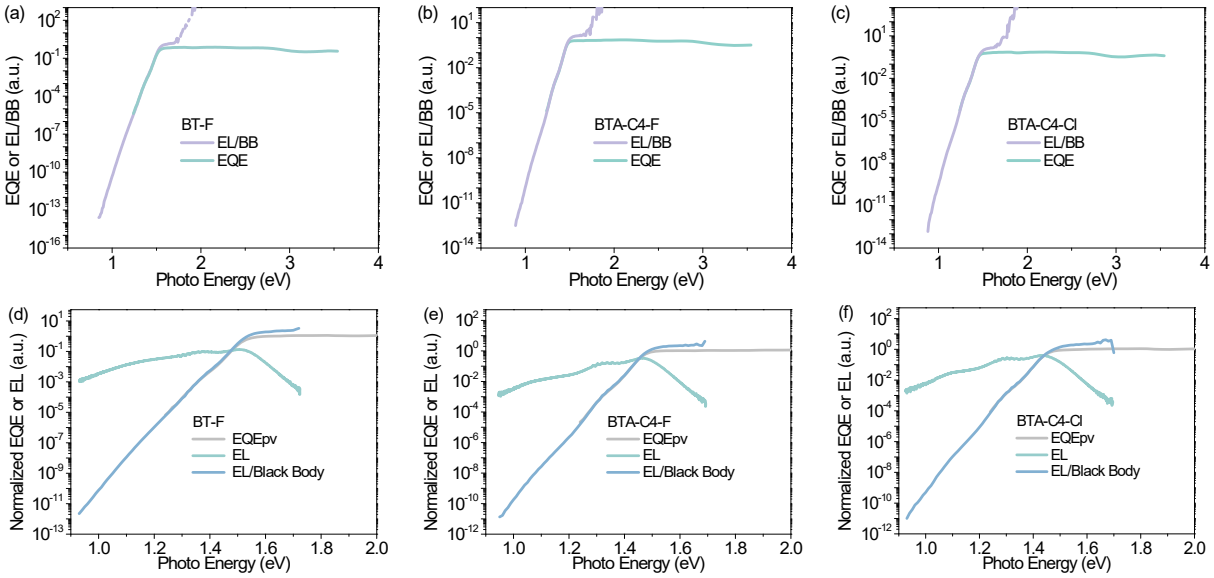

Figure S31. Fourier transform photocurrent spectroscopy (FTPS) and the external quantum efficiency EQE_{EL} extracted from the electroluminescence (ϕ_{EL}) and the black-body emission (ϕ_{bb}) of the OSCs based on (a, d) BT-F, (b, e) BTA-C4-F, and (c, f) BTA-C4-Cl.

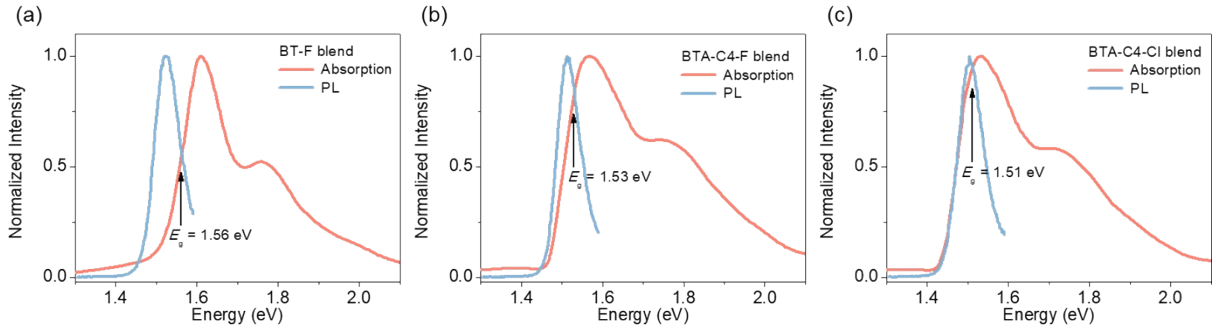

Figure S32. The normalized absorption and photoluminescence spectra of neat acceptor films.

Table S13. Detailed energy loss analysis of the optimal OSCs based on BT-F, BTA-C4-F, and BTA-C4-Cl.

Acceptor	E_g (eV)	$qV_{oc,SQ}$ (eV)	$qV_{oc,Rad}$ (eV)	ΔE_1 (eV)	ΔE_2 (eV)	ΔE_3 (eV)	E_{loss} (eV)
BT-F	1.56	1.287	1.210	0.273	0.077	0.290	0.64
BTA-C4-F	1.53	1.259	1.182	0.271	0.077	0.272	0.62
BTA-C4-Cl	1.51	1.241	1.160	0.269	0.081	0.260	0.61

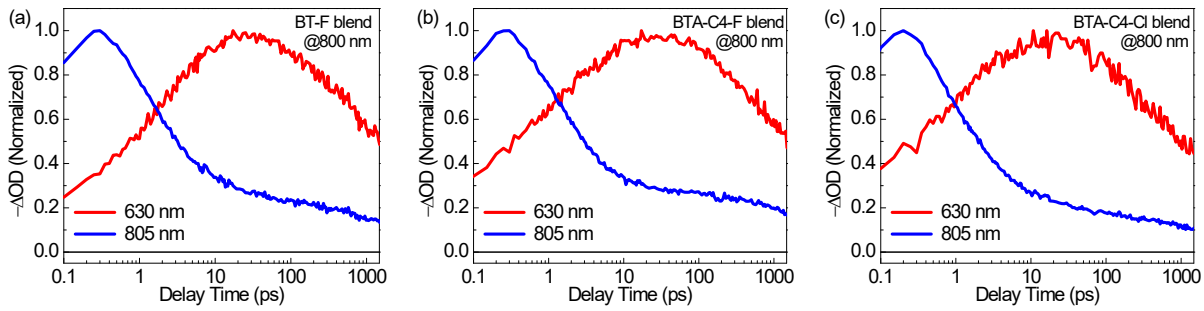

Figure S33. The extracted dynamics at 630 and 805 nm of the blend films based on BT-F, BTA-C4-F, and BTA-C4-Cl under 800 nm excitation.

Table S14. Detailed parameters of hole transfer kinetics within the optimal active layers based on BT-F, BTA-C4-F, and BTA-C4-Cl.

Acceptor	A_1	τ_1 (ps)	A_2	τ_2 (ps)	τ_h (ps) [a]
BT-F	41.7	0.37	58.3	3.37	2.12
BTA-C4-F	58.0	0.31	42.0	3.48	1.64
BTA-C4-Cl	55.6	0.30	44.4	2.25	1.17

a) τ_h can be obtained by the equation: $\tau_h = A_1\tau_1 + A_2\tau_2$

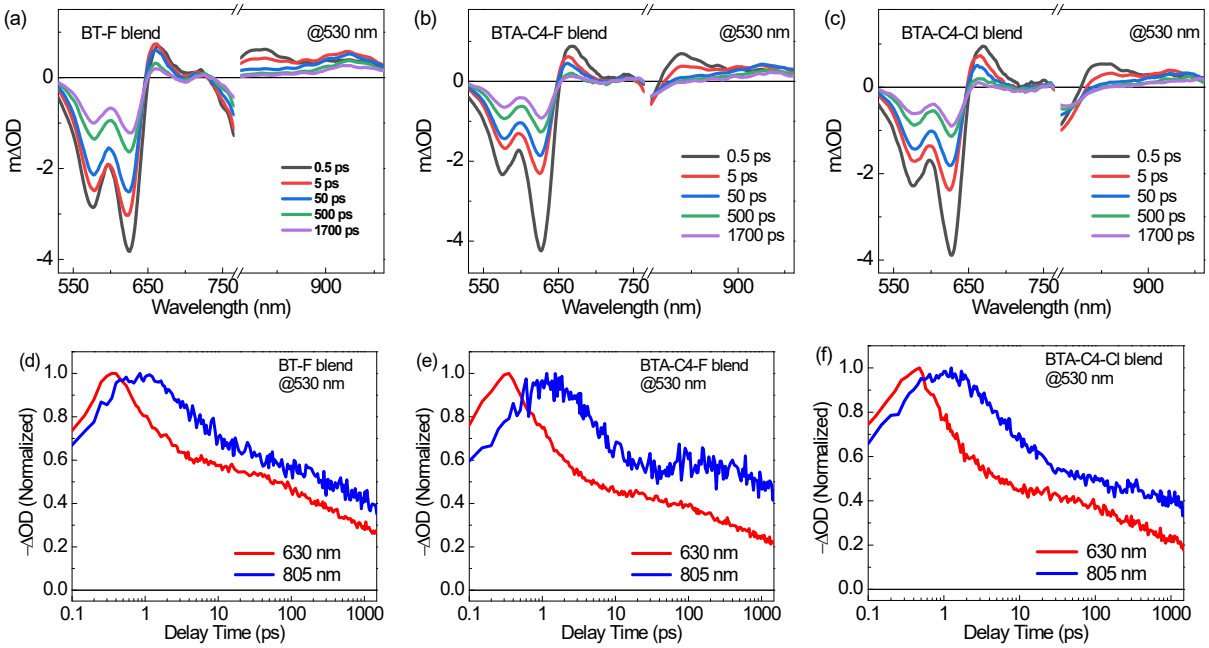

Figure S34. (a–c) TA spectra of blend films under 530 nm excitation at selected delay times. (d–f) The extracted dynamics at 630 and 805 nm of blend films under 530 nm excitation.

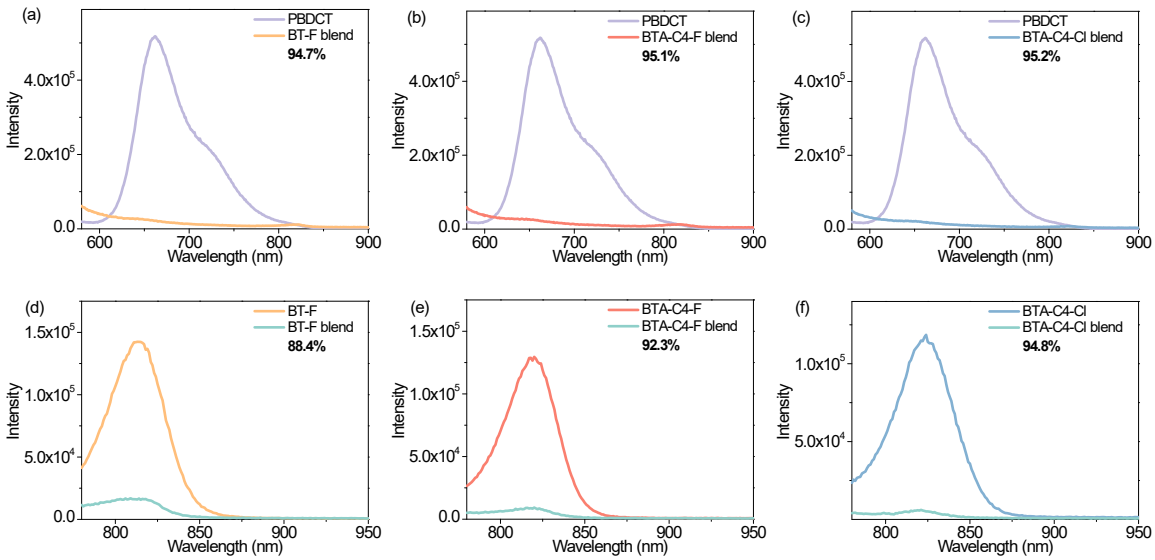

Figure S35. (a–c) PL spectra of neat donor film and blend films excited at 530 nm. (d–f) PL spectra of neat acceptor films and blend films excited at 770 nm.

Table S15. GIWAXS parameters of the blend films of BT-F, BTA-C4-F, and BTA-C4-Cl.

Sample	OOP (010)			IP (100)		
	q ($Å^{-1}$)	*d*-spacing (Å)	CCL (Å)	*q* ($Å^{-1}$)	*d*-spacing (Å)	CCL (Å)
BT-F	1.71	3.67	26.65	0.31	20.27	116.24
BTA-C4-F	1.72	3.65	26.71	0.31	20.27	110.04
BTA-C4-Cl	1.74	3.61	28.20	0.31	20.27	110.68

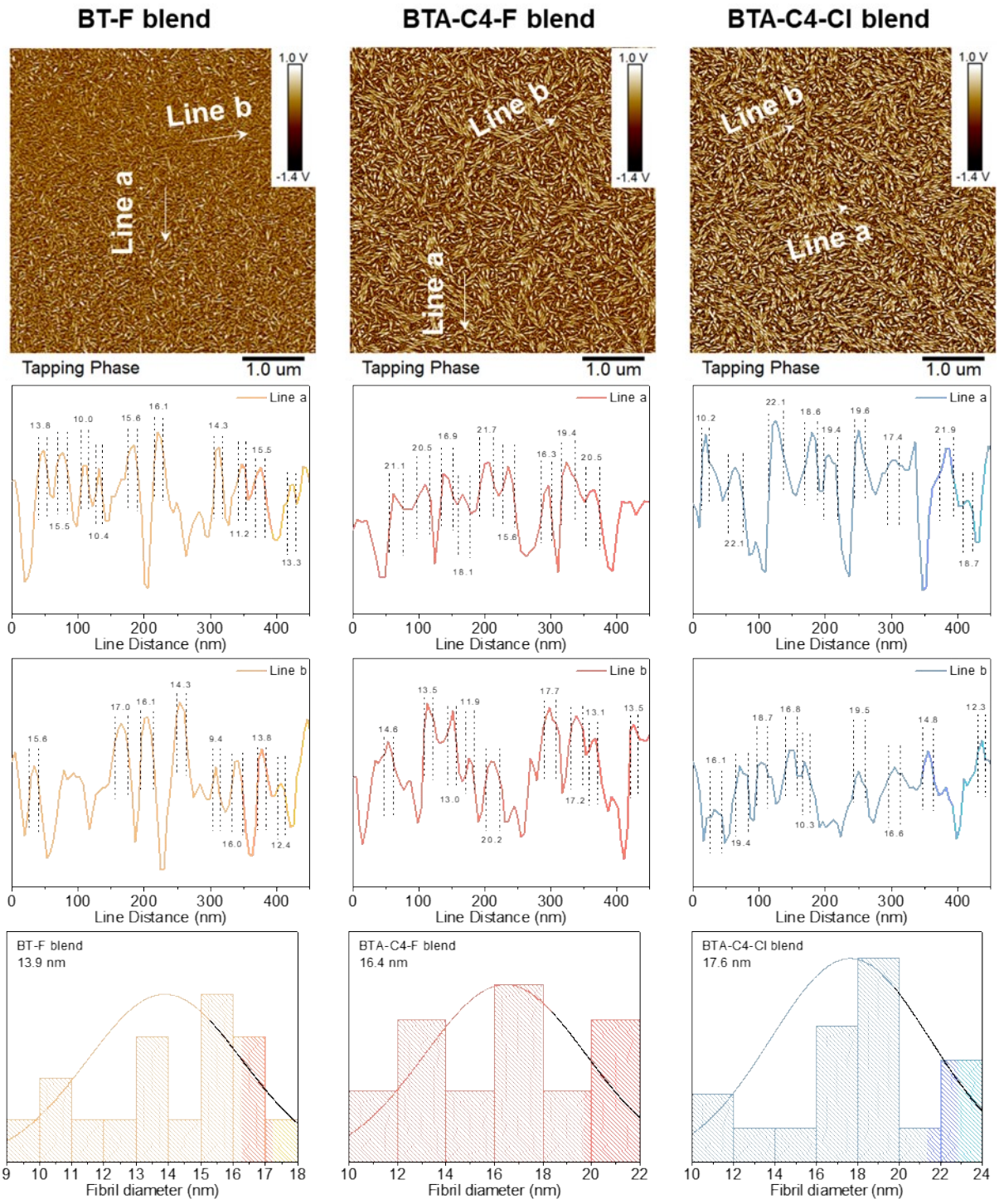

Figure S36. AFM phase images (first row) of the blend films based on BT-F, BTA-C4-F, and BTA-C4-Cl. The line profile to obtain the fibril width (second and third row) and the statistical distribution (fourth row) for the three blend films.

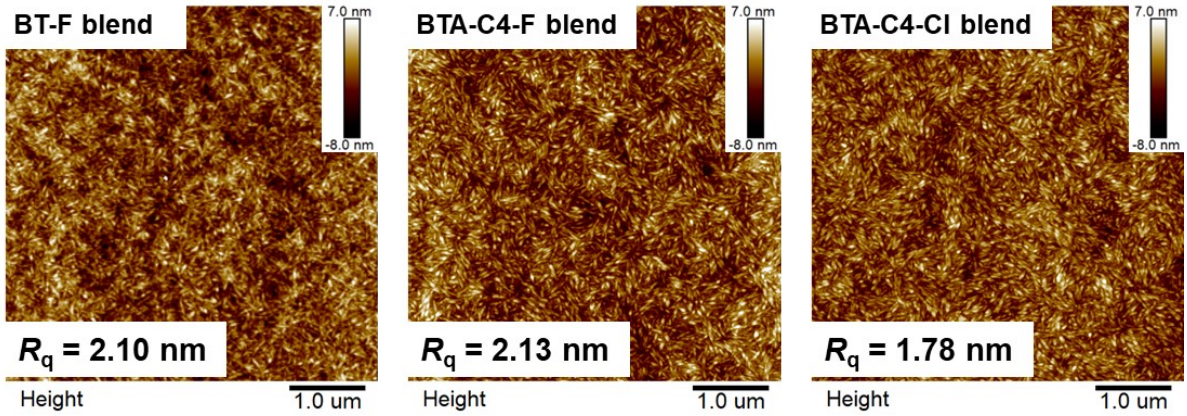

Figure S37. AFM height images of the blend films based on BT-F, BTA-C4-F, and BTA-C4-Cl.

3. Reference

1. Y. Li, Y. Chen, X. Liu, Z. Wang, X. Yang, Y. Tu and X. Zhu, *Macromolecules*, 2011, **44**, 6370-6381.
2. Y. Cho, Z. Sun, K. M. Lee, G. Zeng, S. Jeong, S. Yang, J. E. Lee, B. Lee, S.-H. Kang, Y. Li, Y. Li, S. K. Kwak and C. Yang, *ACS Energy Lett.*, 2023, **8**, 96-106.
3. Z. Wang, W. Wei, L. Zeng, T. Liu, X. Yuan, J. Zhou, B. Yin, J. Li, Z. Xie, F. Huang, Y. Cao and C. Duan, *Chem. Mater.*, 2023, **35**, 6932-6942.
4. X. Yuan, Y. Zhao, T. Zhan, J. Oh, J. Zhou, J. Li, X. Wang, Z. Wang, S. Pang, P. Cai, C. Yang, Z. He, Z. Xie, C. Duan, F. Huang and Y. Cao, *Energy Environ. Sci.*, 2021, **14**, 5530-5540.
5. M. J. Frisch, G. W. Trucks, H. B. Schlegel, G. E. Scuseria, M. A. Robb, J. R. Cheeseman, G. Scalmani, V. Barone, G. A. Petersson, H. Nakatsuji, X. Li, M. Caricato, A. V. Marenich, J. Bloino, B. G. Janesko, R. Gomperts, B. Mennucci, H. P. Hratchian, J. V. Ortiz, A. F. Izmaylov, J. L. Sonnenberg, Williams, F. Ding, F. Lipparini, F. Egidi, J. Goings, B. Peng, A. Petrone, T. Henderson, D. Ranasinghe, V. G. Zakrzewski, J. Gao, N. Rega, G. Zheng, W. Liang, M. Hada, M. Ehara, K. Toyota, R. Fukuda, J. Hasegawa, M. Ishida, T. Nakajima, Y. Honda, O. Kitao, H. Nakai, T. Vreven, K. Throssell, J. A. Montgomery Jr., J. E. Peralta, F. Ogliaro, M. J. Bearpark, J. J. Heyd, E. N. Brothers, K. N. Kudin, V. N. Staroverov, T. A. Keith, R. Kobayashi, J. Normand, K. Raghavachari, A. P. Rendell, J. C. Burant, S. S. Iyengar, J. Tomasi, M. Cossi, J. M. Millam, M. Klene, C. Adamo, R. Cammi, J. W. Ochterski, R. L. Martin, K. Morokuma, O. Farkas, J. B. Foresman and D. J. Fox, *Journal*, 2016.
6. T. Lu and F. Chen, *J. Comput. Chem.*, 2012, **33**, 580-592.
7. R. Po, G. Bianchi, C. Carbonera and A. Pellegrino, *Macromolecules*, 2015, **48**, 453-461.
8. J. Yao, B. Qiu, Z.-G. Zhang, L. Xue, R. Wang, C. Zhang, S. Chen, Q. Zhou, C. Sun, C. Yang, M. Xiao, L. Meng and Y. Li, *Nat. Commun.*, 2020, **11**, 2726.
9. Y. Shi, Y. Chang, K. Lu, Z. Chen, J. Zhang, Y. Yan, D. Qiu, Y. Liu, M. A. Adil, W. Ma,

X. Hao, L. Zhu and Z. Wei, *Nat. Commun.*, 2022, **13**, 3256.
10. L. Feng, J. Yuan, Z. Zhang, H. Peng, Z. G. Zhang, S. Xu, Y. Liu, Y. Li and Y. Zou, *ACS Appl. Mater. Interfaces*, 2017, **9**, 31985-31992.
11. J. Song, F. Cai, C. Zhu, H. Chen, Q. Wei, D. Li, C. Zhang, R. Zhang, J. Yuan, H. Peng, S. K. So and Y. Zou, *Sol. RRL*, 2021, **5**, 2100281.
12. Q. Wei, S. Liang, W. Liu, Y. Hu, B. Qiu, J. Ren, J. Yuan, F. Huang, Y. Zou and Y. Li, *ACS Energy Lett.*, 2022, **7**, 2373-2381.
13. F. Li, Y. Chen, X.-H. Fan, C.-Y. Gao, X. Zhu and L.-M. Yang, *J. Mater. Chem. C*, 2022, **10**, 7724-7730.
14. X. Xu, Q. Wei, J. Song, J. Jing, Y. Chen, F. Huang, X. Lu, Y. Zhou, J. Yuan and Y. Zou, *J. Mater. Chem. A*, 2022, **10**, 24717-24725.
15. S. Zhu, C. Shi, Q. Wei, C. Zhu, J. Ren, J. Li, L. Meng, Y. Li, J. Yuan and Y. Zou, *Chin. J. Chem.*, 2023, **41**, 1815-1822.
16. D. Li, Y. Xu, W. Zhao, G. Cui, G. Li and B. Tang, *Sol. RRL*, 2023, **7**, 2300413.
17. N. Yang, Y. Cui, Y. Xiao, Z. Chen, T. Zhang, Y. Yu, J. Ren, W. Wang, L. Ma and J. Hou, *Angew. Chem., Int. Ed.*, 2024, **63**, e202403753.
18. S. Li, L. Zhan, F. Liu, J. Ren, M. Shi, C. Z. Li, T. P. Russell and H. Chen, *Adv. Mater.*, 2018, **30**, 1705208.
19. J. Wu, Q. Fan, M. Xiong, Q. Wang, K. Chen, H. Liu, M. Gao, L. Ye, X. Guo, J. Fang, Q. Guo, W. Su, Z. Ma, Z. Tang, E. Wang, H. Ade and M. Zhang, *Nano Energy*, 2021, **82**, 105679.
20. H. Fu, J. Yao, M. Zhang, L. Xue, Q. Zhou, S. Li, M. Lei, L. Meng, Z. G. Zhang and Y. Li, Nat. Commun., 2022, **13**, 3687.
21. Y. Ma, M. Zhang, S. Wan, P. Yin, P. Wang, D. Cai, F. Liu and Q. Zheng, *Joule*, 2021, **5**, 197-209.
22. C. Li, J. Zhou, J. Song, J. Xu, H. Zhang, X. Zhang, J. Guo, L. Zhu, D. Wei, G. Han, J. Min, Y. Zhang, Z. Xie, Y. Yi, H. Yan, F. Gao, F. Liu and Y. Sun, *Nat. Energy*, 2021, **6**, 605-613.
23. L. Zhu, M. Zhang, J. Xu, C. Li, J. Yan, G. Zhou, W. Zhong, T. Hao, J. Song, X. Xue, Z. Zhou, R. Zeng, H. Zhu, C. C. Chen, R. C. I. MacKenzie, Y. Zou, J. Nelson, Y. Zhang, Y. Sun and F. Liu, *Nat. Mater.*, 2022, **21**, 656-663.
24. J. Yuan, Y. Zhang, L. Zhou, G. Zhang, H.-L. Yip, T.-K. Lau, X. Lu, C. Zhu, H. Peng, P. A. Johnson, M. Leclerc, Y. Cao, J. Ulanski, Y. Li and Y. Zou, *Joule*, 2019, **3**, 1140-1151.
25. H. Lu, W. Liu, G. Ran, Z. Liang, H. Li, N. Wei, H. Wu, Z. Ma, Y. Liu, W. Zhang, X. Xu and Z. Bo, *Angew. Chem., Int. Ed.*, 2023, **62**, e202314420.
26. L. Ma, S. Zhang, J. Ren, G. Wang, J. Li, Z. Chen, H. Yao and J. Hou, *Angew. Chem., Int. Ed.*, 2023, **62**, e202214088.
27. D. Li, H. Zhang, X. Cui, Y.-N. Chen, N. Wei, G. Ran, H. Lu, S. Chen, W. Zhang, C. Li, Y. Liu, Y. Liu and Z. Bo, *Adv. Mater.*, 2024, **36**, 2310362.